Geophysical Journal International

Geophys. J. Int. (2014) **198,** 1526–1542 doi: 10.1093/gji/ggu193
GJI Seismology

Joint inversion of surface waves and teleseismic body waves across the Tibetan collision zone: the fate of subducted Indian lithosphere

Ceri Nunn,[1] Steven W. Roecker,[2] Keith F. Priestley,[1] Xiaofeng Liang[3] and Amy Gilligan[1]

[1]*Department of Earth Sciences, University of Cambridge, Cambridge, United Kingdom. E-mail: cn277@cam.ac.uk*
[2]*Department of Earth and Environmental Sciences, Rensselaer Polytechnic Institute, Troy, NY, USA*
[3]*Institute of Geology and Geophysics, Chinese Academy of Sciences, Beijing, China*

Accepted 2014 May 20. Received 2014 May 16; in original form 2014 February 13

SUMMARY

We carry out a joint inversion of surface wave dispersion curves and teleseismic shear wave arrival times across the Tibetan collision zone, from just south of the Himalaya to the Qaidam Basin at the northeastern margin of the plateau, and from the surface to 600 km depth. The surface wave data consist of Rayleigh-wave group dispersion curves, mainly in the period range from 10 to 70 s, with a maximum of 2877 source–receiver pairs. The body wave data consist of more than 8000 *S*-wave arrival times recorded from 356 telesesmic events. The tomographic images show a 'wedge' of fast seismic velocities beneath central Tibet that starts underneath the Himalaya and reaches as far as the Bangong–Nujiang Suture (BNS). In our preferred interpretation, in central Tibet the Indian lithosphere underthrusts the plateau to approximately the BNS, and then subducts steeply. Further east, Indian lithosphere appears to be subducting at an angle of ∼45°. We see fast seismic velocities under much of the plateau, as far as the BNS in central Tibet, and as far as the Xiangshuihe–Xiaojiang Fault in the east. At 150 km depth, the fast region is broken by an area ∼300 km wide that stretches from the northern edge of central Tibet southeastwards as far as the Himalaya. We suggest that this gap, which has been observed previously by other investigators, represents the northernmost edge of the Indian lithosphere, and is a consequence of the steepening of the subduction zone from central to eastern Tibet. This also implies that the fast velocities in the northeast have a different origin, and are likely to be caused by lithospheric thickening or small-scale subduction of Asian lithosphere. Slow velocities observed to the south of the Qaidam suggest that the basin is not subducting. Finally, we interpret fast velocities below 400 km as subducted material from an earlier stage of the collision that has stalled in the transition zone. Its position to the south of the present subduction is likely to be due to the relative motion of India to the northeast.

Key words: Tomography; Mantle processes; Body waves; Surface waves and free oscillations; Seismic tomography; Continental margins: convergent; Asia.

1 INTRODUCTION

Many studies have employed teleseismic body wave tomography to generate compressional and shear wave velocity models of the mantle beneath central and eastern Tibet (e.g. Wittlinger *et al.* 1996; Tilmann *et al.* 2003; Li *et al.* 2008; He *et al.* 2010; Hung *et al.* 2010; Liang *et al.* 2011, 2012; Zhang *et al.* 2012a,b). The method is popular because it does not require local seismicity, is relative straightforward to implement and samples deep into the mantle. At the same time, it has well-known limitations (e.g. Rawlinson *et al.* 2010a): (1) structure from outside the region can be mapped into the modelled area, (2) only relative changes in lateral variations in seismic velocity can be determined and (3) shallow structure cannot be resolved. The last limitation can be a particular concern in areas like Tibet where the crust is highly heterogeneous. To prevent shallow heterogeneity being mapped deeper into the model, station corrections are commonly included as unknowns in the inversion (e.g. Frederiksen *et al.* 1998; Graeber *et al.* 2002) but this does not enhance resolution of shallow structure (Rawlinson & Kennett 2008), and heterogeneity in regions with gradual boundaries and large lateral extent can be attenuated in the resulting model (Priestley & Tilmann 2009). Alternative approaches include incorporating existing models of shallow structure (e.g. Abers & Roecker 1991; Waldhauser *et al.* 2002; Martin *et al.* 2005; Lei & Zhao

2007; Nunn *et al.* 2014); simultaneously inverting data from local and teleseismic earthquakes (Shedlock & Roecker 1987); and simultaneously inverting 3-D wide-angle data and teleseismic data (Rawlinson *et al.* 2010b).

Surface wave tomography has also been used in many studies of Tibet and surrounding regions, using signals generated by earthquakes (Cotte *et al.* 1999; Shapiro & Ritzwoller 2002; Rapine *et al.* 2003; Priestley *et al.* 2006; Acton *et al.* 2010; Feng *et al.* 2011; Ceylan *et al.* 2012) and ambient noise (Yang *et al.* 2012). In contrast to teleseismic body wave tomography, surface wave tomography generally has good depth resolution. Depth resolution diminishes as depth increases, and depends on the range of periods used and whether the overtones are also included. Lateral resolution is limited by the minimum wavelength of the signal, and so also diminishes with depth.

The complementary sensitivities of teleseismic shear waves to lateral variations and surface waves to vertical variations provide a compelling motivation for combining these observations in a joint inversion. For example, West *et al.* (2004) show that the retrieval of a variety of structures is much improved when using a joint approach. A number of researchers have carried out joint inversions of body and surface wave data on a global scale (e.g Mégnin & Romanowicz 2000; Antolik *et al.* 2003; Lebedev & van der Hilst 2008). On a regional scale, Rawlinson & Fishwick (2012) used surface waves to account for the long-wavelength structure that is filtered out when relative traveltime residuals are used with transportable arrays. West *et al.* (2004) used surface waves as horizontally propagating rays with deep sensitivity kernels in order to invert them jointly with body waves along a linear array. Friederich (2003) combine shear waves with surface waveforms in East Asia, and Schmid *et al.* (2008) jointly invert surface waves [using the partitioned waveform inversion method of Nolet (1990)] and regional and teleseismic *S* waves in Europe. Finally, joint inversions of body wave traveltimes and surface wave phase velocities have been carried out in the western United States and China (Obrebski *et al.* 2011, 2012) .

In this study, we carry out a 3-D joint inversion that covers the entire collision zone across much of central and eastern Tibet. In order to take advantage of the wide distribution of stations (as opposed to linear arrays) providing body wave data, the joint inversion method uses maps of surface wave group velocity across the region. We use no station terms and make no *a priori* crustal correction, but instead allow the surface wave observations (within the joint inversion) to constrain a crustal model to correct for traveltimes at shallow depths.

2 GEOTECTONIC SETTING

At the surface, the Tibetan plateau is a relatively uniform area of ∼5 km elevation. Its formation involved numerous collisions, and several major sutures formed during the closure of the Tethys ocean (Fig. 1). Based on a change in plate motion, most researchers suggest collision between India and Eurasia probably began 50–55 Ma (e.g. Molnar & Tapponnier 1975; Patriat & Achache 1984; Copley *et al.* 2010), although Yin & Harrison (2000) suggest it could have started as early as latest Cretaceous time (∼70 Ma) and Aitchison *et al.* (2007) prefer a later collision time of ∼34 Ma. There are many fault systems within Tibet, with north–south oriented rifts in the south, major thrusts at the Himalaya, thrust systems bounding the Qaidam, and an abundance of major strike-slip faults. The crust is more than 70 km thick under much of the plateau (Kind *et al.* 2002; Yue *et al.* 2012). The 3-km-high Qaidam is the largest basin within the plateau, with a total crustal thickness of ∼50 km (Karplus *et al.* 2011; Yue *et al.* 2012).

Despite many geophysical investigations, there remains considerable disagreement regarding the processes involved in building the plateau [see Mechie & Kind (2013) for a review]. Many authors consider that India subducts underneath the plateau to approximately the Bangong–Nujiang Suture (BNS; e.g. Friederich 2003; Tilmann *et al.* 2003; Li *et al.* 2008; Feng *et al.* 2011; Liang *et al.* 2012), but Obrebski *et al.* (2012) infer that India underthrusts as far as the Jinsha Suture, and Priestley *et al.* (2006) suggest that India underthrusts the entire plateau. Tilmann *et al.* (2003) consider the subducted lithosphere to be dipping almost vertically, Obrebski *et al.* (2012) find the dip to be shallow, while others infer intermediate dips (e.g. Liang *et al.* 2012). Liang *et al.* (2011) use north-dipping lineations in the mantle to suggest that the Indian Plate has subducted in a stepped, piecewise fashion. Some studies have observed a break in the fast velocities underlying much of southern Tibet (e.g. Ren & Shen 2008; Liang *et al.* 2011). Ren & Shen (2008) interpret the low-velocity gap as evidence of asthenospheric upwelling, which is then responsible for the north–south rifting in southern Tibet. Alternatively, Liang *et al.* (2012) suggest that the low-velocity gap is unrelated to surface rifting and is caused by fragmentation in the Indian Plate. In addition to these various disagreements, studies of the entire collision zone show that it is not uniform from west to east (Li *et al.* 2008; Agius & Lebedev 2013).

3 DATA AND METHODS

3.1 Body wave data

We use *S*-wave arrival times collected in the 0.05–0.5 Hz frequency range by Liang *et al.* (2012). These arrivals are recorded at 237 stations (Fig. 2a) from the Hi-Climb, HIMNT, INDEPTH II, INDEPTH III and INDEPTH IV/ASCENT, Namcha Barwa and PASSCAL91 projects as well as stations in Bhutan and the Global Seismic Network (GSN). We make internetwork measurements where possible, and additionally use the permanent GSN station at Lhasa as a common reference point.

Events occurring within 27°–85° of the study area which were recorded by at least four stations (Fig. 2b) were selected for analysis. After initial manual picking of phases, relative arrival times were estimated using Multi-Channel Cross-Correlation (MCCC; VanDecar & Crosson 1990). We use a total of 8665 paths, providing the ray coverage shown in Fig. 3. To provide an estimate of measurement error we searched for pairs of observations where events within 10 km of each other were observed at the same station. 126 of these event pairs have at least one pair of stations recording both events, providing a total of 6841 paired observations and an rms estimate of 0.3 s (Fig. 2c).

3.2 Surface wave data

The surface wave observations are measurements of fundamental mode Rayleigh-wave group velocity dispersion. 11 per cent of the data are from Gilligan *et al.* (in press), 51 per cent from Acton *et al.* (2010) and the remainder are new data generated for this study (Fig. 4a). The new data were recorded by 92 stations from ASCENT/INDEPTH IV, plus two permanent stations from the Global Seismograph Network (Fig. 4a). Seismograms from 49 earthquakes with $M_w > 5.0$ and located between 23°and 58°N and 69° and 121°E (Fig. 4a) densify the coverage of the region. Of the

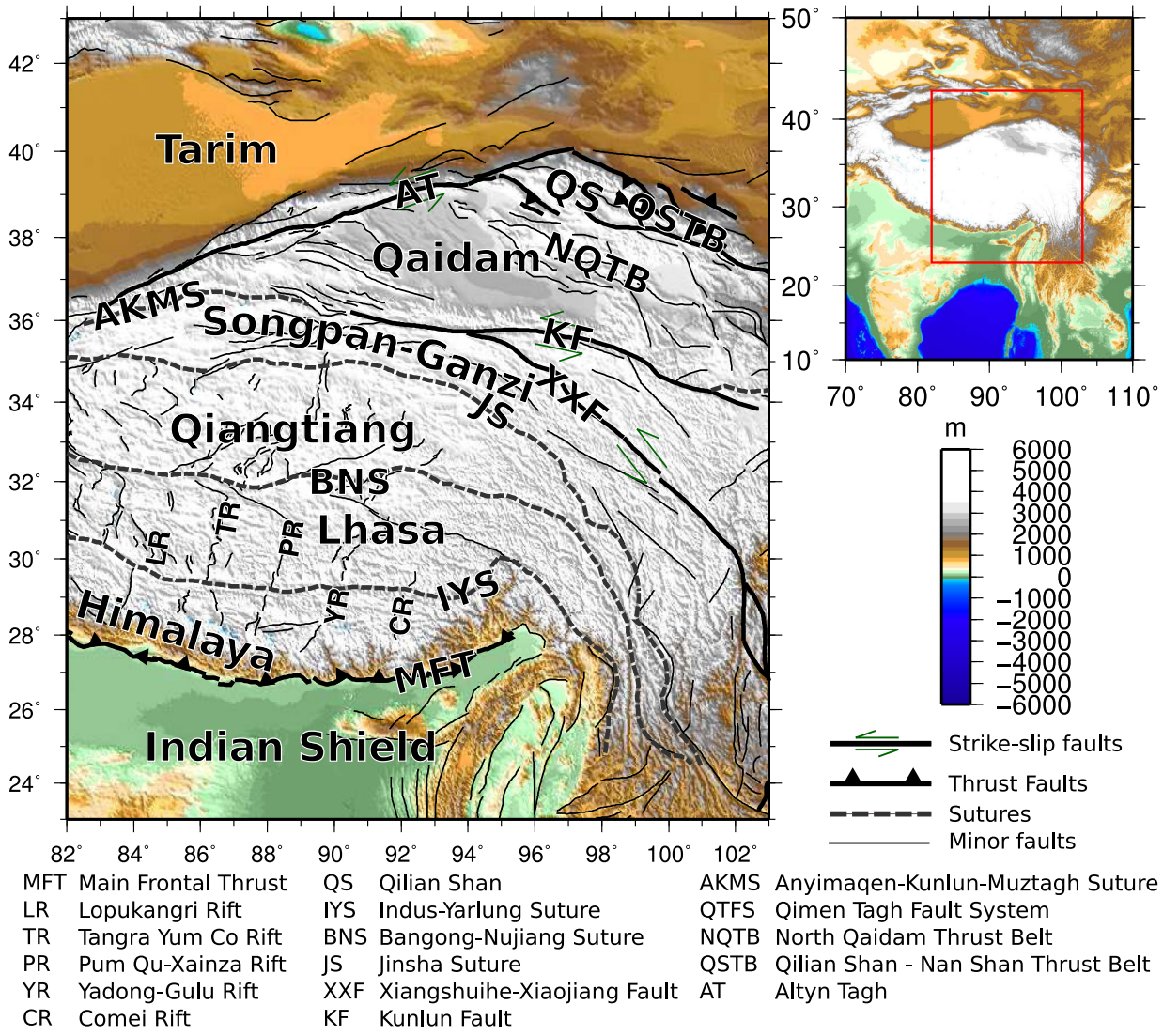

Figure 1. Map of the study region showing terranes, major faults (black lines) and sutures (dashed grey lines). Barbed lines are thrusts, and slip direction is indicated in green on strike-slip faults. Geological structures are from the HimaTibetMap-1.1 data set (Styron *et al.* 2010), based on Taylor & Yin (2009).

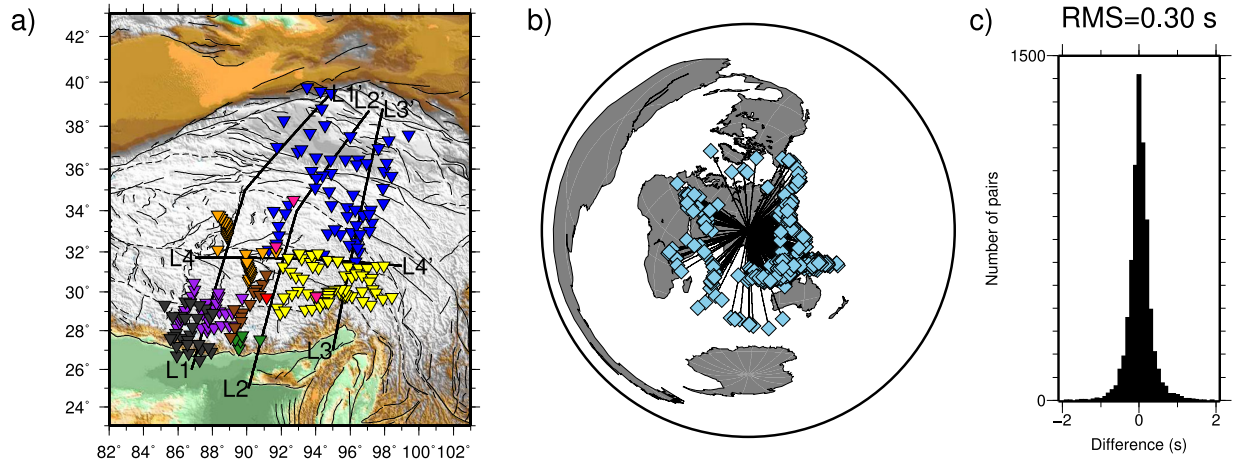

Figure 2. Sources of body wave data. (a) Triangles locate stations from the following networks: X4-ASCENT (blue), XR-INDEPTH III (orange), XR-INDEPTH II (brown), XE-Namchabawa (yellow), XF-Hi-CLIMB (purple), YL-HIMNT (grey), XA-BHUTAN (green), XC-PASSCAL91 (pink) and IC-GSN (red). Black lines show profiles L1, L2, L3 and L4 used in later figures. (b) Locations of 356 teleseismic events (blue diamonds) that provided 8665 *S*-wave arrivals. (c) Histogram showing the difference between the relative traveltimes for pairs of events within 10 km of each other observed at the same station. The standard deviation of this plot provides an estimate of measurement error. The data were previously published in Liang *et al.* (2012).

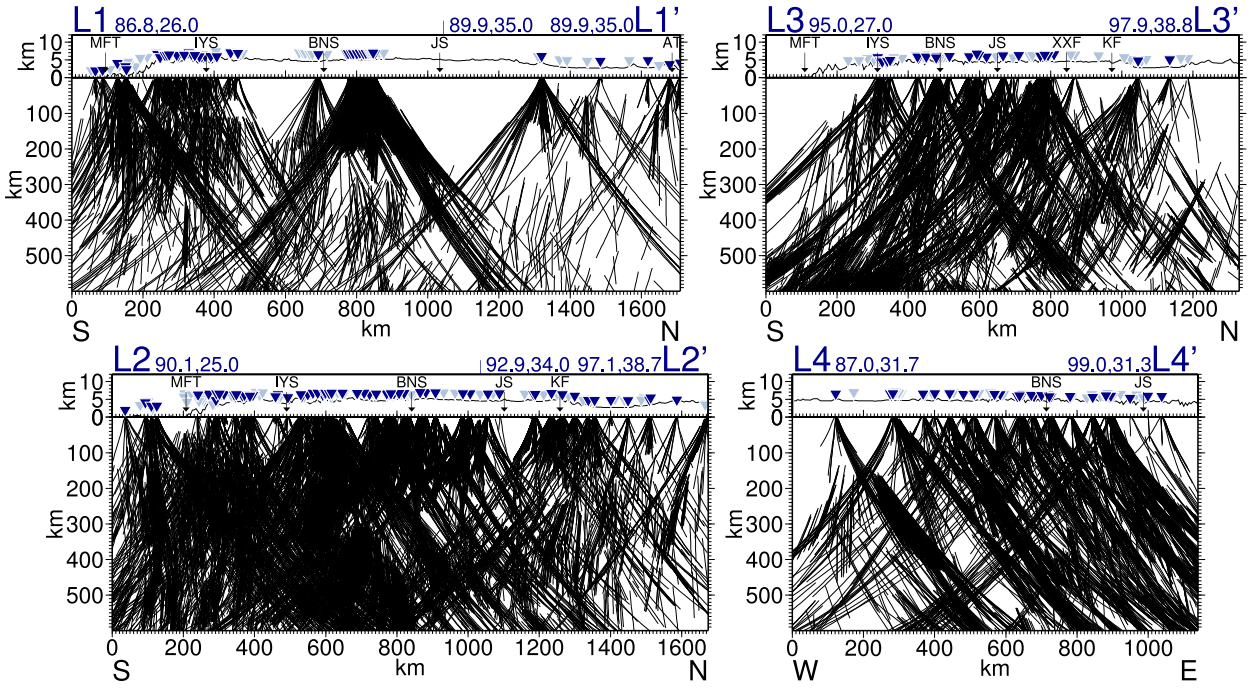

Figure 3. Body wave ray coverage along profiles L1, L2, L3 and L4 (Fig. 1). Ray paths are shown within 60 km of each profile. Topography, major faults and sutures are projected onto the profile, along with stations within 60 and 150 km of the profile (dark and light blue triangles, respectively). Only those stations that provide body wave data are included.

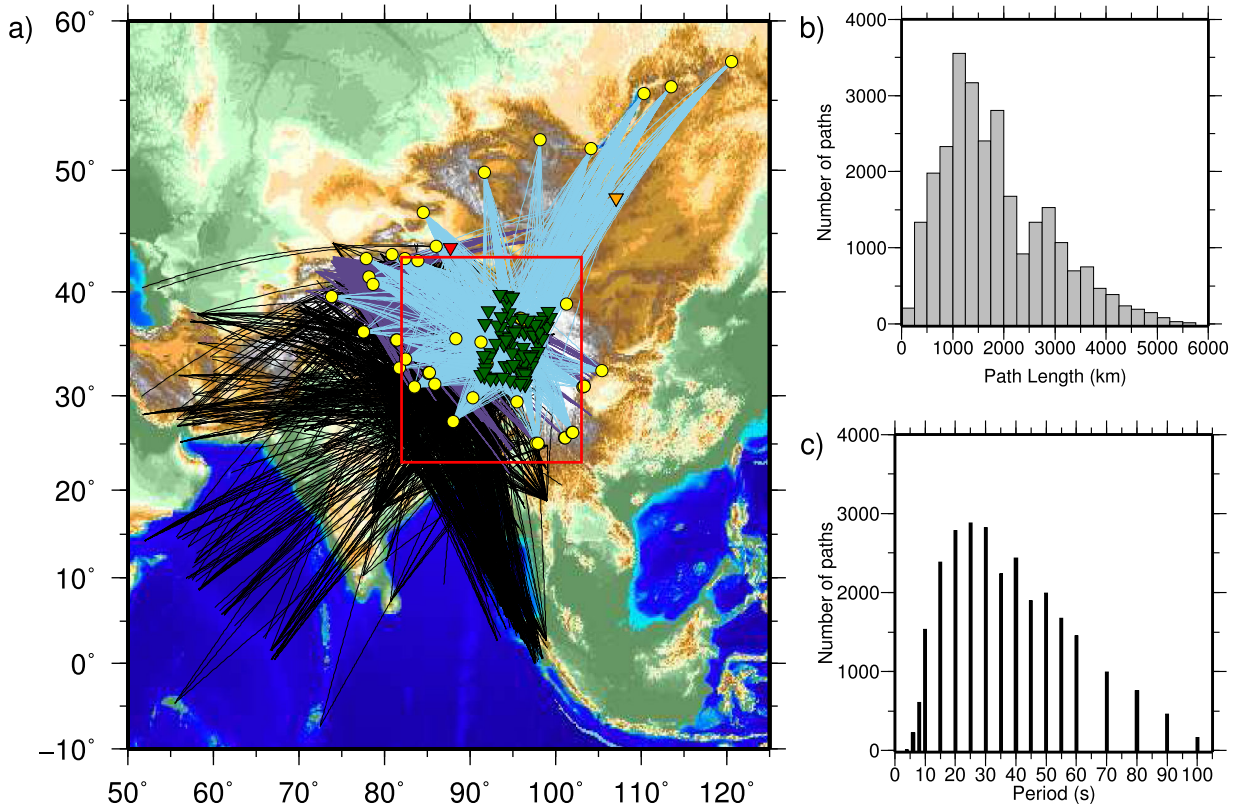

Figure 4. Surface wave observations. (a) Path coverage map for 25 s period fundamental mode Rayleigh-wave group velocity data. The red box locates the study area. Yellow circles are earthquakes, triangles are seismic stations. Green triangles are INDEPTH IV/ASCENT stations; red and orange triangles are GSN stations WMQ and ULN, respectively. Blue lines are great circle paths of new Rayleigh-wave observations. Purple and black paths represent data from Gilligan *et al.* (in press) and Acton *et al.* (2010), respectively. (b) Path length distribution of the data. The average path length is 1836 km. Including all periods, there are a total of 27292 surface wave observations [10446 from this study, 3036 from Gilligan *et al.* (in press), and 13810 from Acton *et al.* (2010)]. (c) Frequency distribution of the data.

observations taken from Acton *et al.* (2010), 20 per cent are from clustered data, meaning that, for each period, measurements from paths whose endpoints lay within 4 per cent of the path length of each other are grouped to produce a cluster with the mean properties of the constituent paths.

The three data sets were processed in the same way. The vertical component is corrected for instrument response, decimated to 1 sample per second and bandpass filtered between 0.01 and 0.2 Hz. Noisy traces were removed after visual inspection: retained traces typically have a signal-to-noise ratio >20. Path lengths are well distributed between ∼80 and ∼5500 km, with a mean path length of ∼1835 km (Fig. 4b). Only a few paths are <250 km, and these are for the shorter periods. There are at least 750 paths for each of the periods analysed between 10 and 70 s (Fig. 4c), with a maximum of 2877 paths for the 25 s period. Smaller numbers of paths are available between 4–8 s and 80–100 s.

3.3 Group velocity determination

Group velocity dispersion curves were calculated as described in Acton *et al.* (2010), using the multiple filter taper analysis (MFT) of Hermann & Ammon (2002). For the new data, traveltimes were determined using origin times and epicentral locations taken from the USGS/NEIC PDE catalogue. The fundamental mode was manually selected to isolate it from its overtones, body waves and multipath surface waves. Phase-matched filtering was then applied, and the fundamental mode reselected on the filtered trace.

Significant lateral variations in structure, such as the Himalayan collision zone, can result in multipathing and refraction of surface waves. We assume that great circle propagation is reasonable for path lengths <5000 km (Ritzwoller *et al.* 2002), and reduce the influence of multipathing by visual inspection of the fundamental mode and phase-matched filtering. Refraction can still be a source of error, particularly at shorter periods. However, average path lengths at the short periods are smaller (e.g. ∼1130 km for 10 s periods and below, compared to ∼1900 km for periods greater than 10 s) and hence less susceptible to multipathing.

As mentioned, Acton *et al.* (2010) clustered dispersion curves from similar paths. The average cluster error was in the range 0.02–0.04 km s^{-1}, and was not strongly dependent on frequency. From the clustered data, we estimate the uncertainty in the observed group traveltimes to be about 1.3 per cent.

3.4 Group velocity tomographic inversion

As a prelude to the joint inversion, we create maps of surface wave group velocities for a range of periods (Fig. 5: top row). The modelled region is parametrized with a mesh of 2-D triangles with sides 1° long. At this initial stage we define a region large enough to include all the stations and receivers (Fig. 4a) and use the 2-D tomographic code of Mitra *et al.* (2006) to calculate the group slowness for each node from dispersion measurements on intersecting propagation paths. Values within each triangular area are determined using three-point interpolation.

To stabilize the inversion, we follow Acton *et al.* (2010), and set the *a priori* constraint on the standard deviation of the slowness across a 10° reference distance. This parameter controls smoothness in order to prevent artefacts that can appear when detail is too fine. Acton *et al.* (2010) set this parameter for each period by subjectively judging the trade-off between model variance, misfits, smoothness and the resolution of known features. The preferred values were 0.07 for 4–8 s, 0.06 for 10–15 s, 0.04 for 20–30 s and 0.06 for 35–100 s, which results in finer detail at short periods (Fig. 5, top row). Fig. 5 (bottom row) shows the fit to the group velocity observations achieved after the joint inversion.

3.5 Joint inversion method

As discussed, the complementary sensitivities of teleseismic shear waves and surface waves provide a compelling motivation for combining the two in a joint inversion. West *et al.* (2004) combined these two types of observation by converting phase velocities to frequency-dependent traveltimes. They applied this idea to differences in phase observed by a local array, which works well for linear arrays recording events along a great circle path aligned with the array azimuth. The paths used in this study are distributed throughout the modelled region, so this approach is extended to incorporate information provided by maps of Rayleigh-wave group velocity determined from regional analyses of surface waves. In this study we use group velocities, although this approach would apply equally to phase velocities. The objective is to construct a model that is consistent with both regional observations of surface wave dispersion curves and observations of teleseismic shear wave arrival times.

A locally defined medium with a heterogeneous distribution of V_s is parametrized by specifying velocities at a set of discrete elements (gridpoints). Intragrid velocities are determined by trilinear interpolation. Body wave traveltimes within the regional model are computed using the finite difference eikonal equation solver of Hole & Zelt (1995), adapted for teleseisms and spherical coordinates by Li *et al.* (2009). We calculate traveltimes from any seismic station to the base of the model, and add this time to a traveltime from the hypocentre to the base of the model derived from standard traveltime tables. The correct time is determined by a grid search for the minimum of the sum of the two times. Following standard practice in arrival time tomography, an inverse problem is constructed by expanding the observed traveltime about the current estimate of the model V_S:

$$t_{\rm obs} = t(v_S) + \sum_i^n \frac{\partial t}{\partial v_i}\Delta v_i, \qquad (1)$$

where the sum is taken over all gridpoints. In the teleseismic case the above equation is demeaned to compensate for ignorance of event origin time and velocities outside the model. A consequence of removing the mean is that teleseismic shear wave traveltimes are insensitive to absolute values of V_S.

For surface waves, the observation is a group traveltime. If the surface wave path is entirely within the modelled region (shown by the red box in Fig. 4a), we use the observed traveltime. If only part of the path is within the region, we construct maps of group velocity $u_\omega(x, y)$ at a range of periods ω (see Section 3.4) and extract the time for that portion of the path (Fig. 6) by integrating

$$t_{\rm obs}(\omega) = \int_a^b \frac{\partial l(x,y)}{u_\omega(x,y)}, \qquad (2)$$

where, if either or both the source and receiver are external to the model, a and b are the points at which the surface wave enters and exits the model (making the assumption that if follows the great circle path). This approach has the advantage of taking into account the distribution of observations used to make the group velocity maps (essentially providing a ray density). It also means that surface wave observations can cover the entire region of interest without increasing the required size of the model (which can be computationally

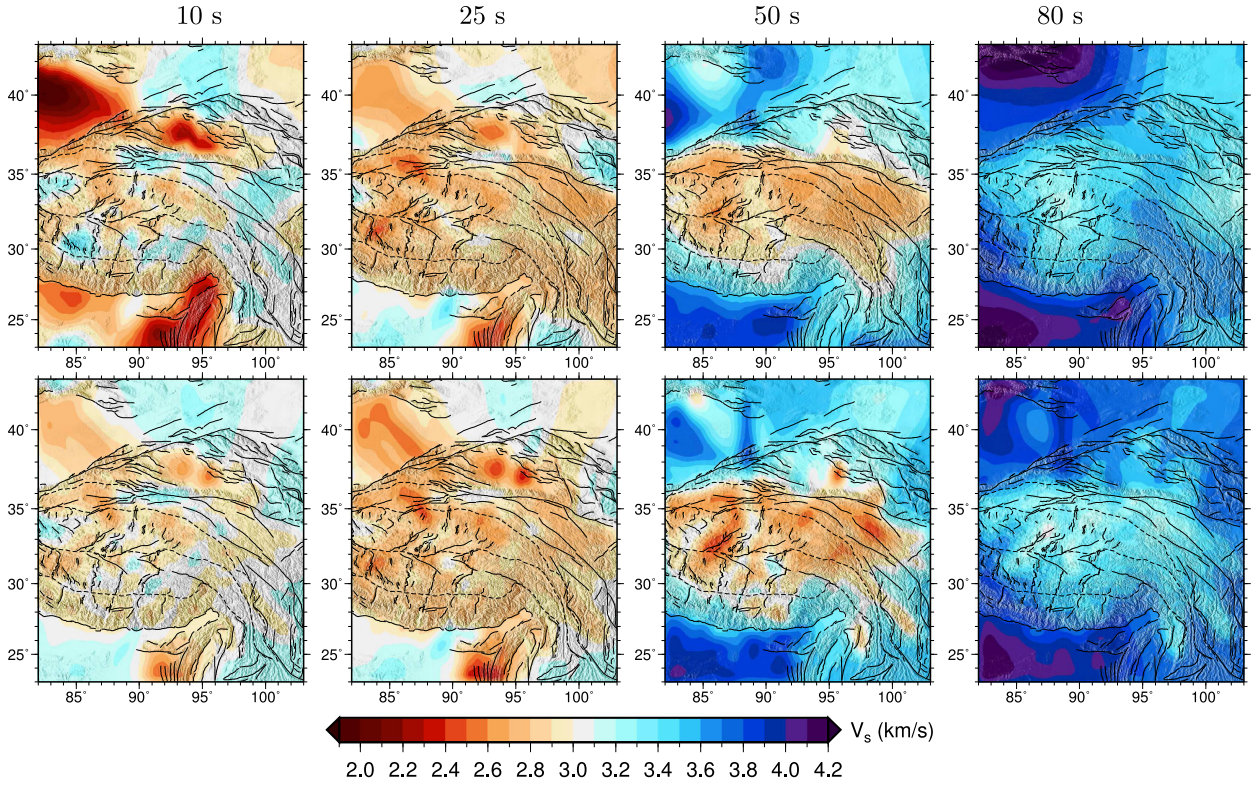

Figure 5. Group velocity maps at 10, 25, 50 and 80 s period used in the joint inversion. The top row shows group velocity maps constructed from the raw surface wave dispersion data using the surface wave tomography algorithm of Mitra *et al.* (2006). These maps are used to generate the group traveltimes in eq. (2). The bottom row shows the fit achieved with the joint inversion.

expensive). An essential assumption behind this approach is that heterogeneity in the group velocity maps is resolvable at the scale of the modelled area.

The surface wave part of the inverse problem is constructed from eq. (2) using the chain rule

$$t_{\rm obs}(\omega) = t(u_\omega(v_s)) + \sum_{i,j} \frac{\partial t}{\partial u_{ij}} \sum_k \frac{\partial u_{ij}}{\partial v_{ijk}} \Delta v_{ijk} \Big|_\omega , \qquad (3)$$

where $u_\omega(v_s)$ is the group velocity map for period ω corresponding to the current V_s model, and the sums are over all areal points (i, j) and depths (k). An implicit assumption in eq. (3) is that a 3-D V_s model can be constructed by combining 1-D models at each point (i, j) (see Montagner 1986). With this assumption, we can construct the group velocities $u_\omega(v_s)$ and the partial derivatives in eq. (3) using the locked-mode method of Gomberg & Masters (1988).

We weight eqs (1) and (3) by observational uncertainties. For body waves we use the estimated uncertainty in the *S*-wave arrival time. For the surface waves, a traveltime uncertainty for each path is estimated from maps of group velocity uncertainties derived from the 2-D inversions. The combined system of linear equations is solved iteratively using the LSQR algorithm of Paige & Saunders (1982). The resulting perturbation dV_s is added to the current V_s to generate a new model, and the process is repeated until reduction in the variance of residuals is insignificant.

3.6 Tuning the joint inversion

We conducted a series of tests using synthetic data to estimate values for a variety of parameters that tune the joint inversion. Synthetic group arrival times and body wave traveltimes used in these tests were calculated using the same procedure as the real data (Section 3.5).

Two model grids are defined: a fine spaced grid for the finite-difference computation of the body wave traveltimes and ray paths, and a coarser grid of adjusted velocities for the joint inversion. Values on the fine spaced grid are determined from those on the coarse grid by trilinear interpolation. We choose a fine grid with 5 km vertical and 0.0625° (∼7 km) horizontal spacing, and a coarse grid with 25 km vertical and 0.25° (∼27 km) horizontal spacing. The depth range is from 10 km above sea level (stations are embedded in the model) to 600 km depth. Velocity perturbations are smoothed over five nodes laterally, but not vertically. We generate a starting model by smoothing the velocity discontinuities in global velocity model *ak135* (Kennett *et al.* 1995) ('Smoothed' *ak135*).

To stabilize the inversion and mitigate the introduction of short-wavelength artefacts, the least-squares solution is damped and short-wavelength perturbations are smoothed using a moving average window prior to modifying the existing model (e.g. Li *et al.* 2009). We determine a damper by experimenting with a range of values, and observing the trade-off between rms and model roughness (Fig. 7). An optimal damper is defined as one that leads to stable convergence and a simple model while fitting the observations reasonably well. Based on these tests, damping was set to 400 and 150 s^2 km^{-2} for the body wave and surface wave inversions, respectively.

We also choose a relative weighting of surface and body wave observations, in such a way that the fit to one type of observation is not overly dominant. Based on a series of checkerboard tests using a range of scaling factors, the surface wave derivatives were scaled by a factor of 4 (Fig. 8). This factor was chosen by comparing the residuals and also by visually inspecting the checker recovery at all depths. Note that for the chosen damping and scaling factors, the

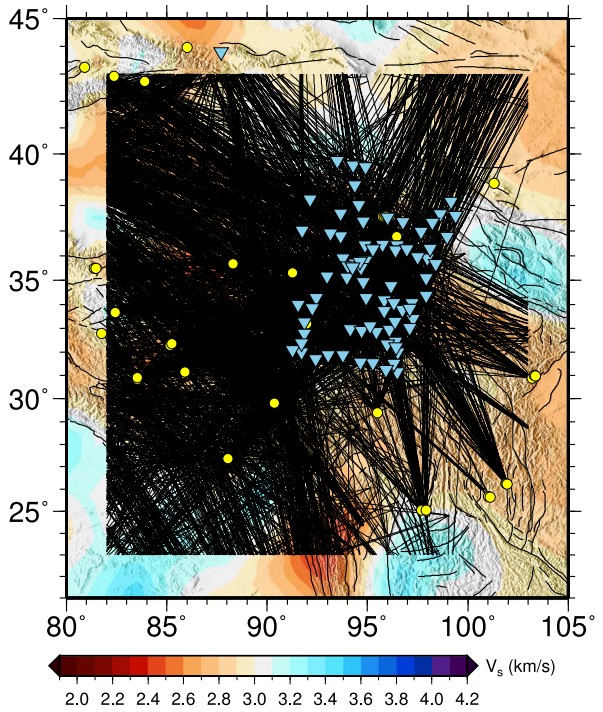

Figure 6. Surface wave path coverage for 25 s period waves within the modelled region. Surface wave paths that intersect the study area are used to calculate group traveltimes for each period from the group velocity map. Yellow circles are earthquakes, and blue triangles are stations (only those earthquakes and stations for the new data used in this study are shown).

residuals for the checkerboards for the joint inversion are lower than for either the body waves or surface waves alone (Fig. 9).

As expected, the surface wave inversions resolve only the shallow checkers (Fig. 8b), while the body wave inversions retrieve checkers at all depths (Fig. 8c). The checkers are well defined where their crossing ray coverage is dense, and there is significant smearing where the ray paths do not cross. For this particular test, which has high-amplitude structures with strongly defined lateral boundaries, the joint inversion did not significantly improve the recovery of the checkers, but nevertheless shows good retrieval of checkers at all depths.

Resolution at shallow depths is governed mainly by the crossing ray coverage of the surface waves (Fig. 6), which explains the significant smearing in the north and east of the model (Fig. 8e). Resolution at depths greater than 175 km is solely determined by the body wave paths, with larger areas being well resolved as depth increases (Figs 8e–h). We note that both the surface wave and joint inversions overestimate the maximum amplitude of checkers. Although the surface waves are able to recover the average velocity (down to ∼125 km), they have some difficulty recovering sharp changes in the velocity depth profile. In our case, small errors in the velocity depth profile result in an overestimation of the checkerboard pattern. For a brief discussion, see Fig. S2. Applying greater damping did not reduce the problem: a similar overestimation of the checkerboard amplitude was observed after the model had converged.

We apply the moving average window smoothing to lateral, but not vertical, variations in the perturbations. We find that vertical smoothing, along with allowing the model to update at all depths, can introduce artefacts into both the surface wave and joint inversions. For example, we carried out synthetic tests with a trial model composed of a thickened crustal layer over a half-space (Fig. 10a). A model recovered using vertical smoothing and updated at all depths shows fast-velocity artefacts in the half-space at depths greater than 100 km (Fig. 10b). Partial derivatives for the range of periods we analyse (Fig. 11) indicate that sensitivities are highest at shallow (to ∼30 km) depths. Sensitivities reduce gradually below this depth, with almost no sensitivity below 200 km.

Results from a series of numerical experiments suggest that these artefacts can be minimized by removing vertical smoothing (Fig. 10e) and initially updating the model only where sensitivities are highest (the upper 100 km). The depth range is gradually increased to 150 km and 200 km as the improvement to the fit to residuals becomes insignificant. This procedure essentially applies a large damper to variables with low sensitivities so that they are not perturbed by potentially large residuals (Figs 10b and c). We also note that simply removing the smoothing (Fig. 10c), or initially only updating at shallow depths (Fig. 10d), did not on their own resolve the problem. We conclude that anomalous structures can be introduced either by oversmoothing, or by allowing updates when residuals are large and the partial derivatives are small.

Additional synthetic tests for likely structures within the modelled area (Fig. 12) are discussed along with the main results below.

4 JOINT INVERSION MODEL: RESULTS AND DISCUSSION

The joint inversion model of the shear wave velocities shows significant variation across central and eastern Tibet (Figs 13 and 14). We discuss the major features of this model in detail below.

4.1 Structure of the crust and uppermost mantle

With a node spacing of 20 km, the variation of seismic velocities at shallow depth will most likely be undersampled in the model. Nevertheless, the shape of the velocity contours indicate thickened crust beneath the plateau and a shallower Moho beneath the Qaidam (Figs 13b, e, h and k). Acton *et al.* (2010) note a correspondence between the depth to the Moho estimated from receiver functions and the 4.1 km s^{-1} velocity contour across much of the region. Where we have information from receiver functions, we also observe a close correspondence between this contour and the Moho estimates (Figs 13b, e, h and k).

The thickened crust exhibits slower than normal velocities for continental crust across the whole plateau. In addition, at 75 km depth, nearly the entire northern plateau (from half-way between the IYS and BNS) is as much as 5 per cent slower than the southern plateau (Fig. 14a). The slowest velocities are in the central section of the northern plateau, and this is also evident at 100 km depth (Fig. 14b). There are also slower velocities just to the north of the MFT along profile L2 (Figs 13d and 14a). McKenzie & Priestley (2008) attribute the shallow low velocities to radiogenic heat production in the thickened mid-crust, which eventually heats the lower crust and the uppermost mantle. Studies of S_n propagation indicate that S_n energy is more strongly attenuated in the northern plateau in comparison to the south (Ni & Barazangi 1983; McNamara *et al.* 1995). Barron & Priestley (2009) investigated the propagation of the S_n phase over a range of frequencies. At the higher frequencies, they similarly observed that the phase was blocked in the northern plateau (Fig. 15a). In the mid-range frequencies, they observed blockage only in the north-central region (Fig. 15b), and efficient propagation at lower frequencies (Fig. 15c). The S_n phase requires a positive downward velocity gradient (Stephens & Isacks 1977),

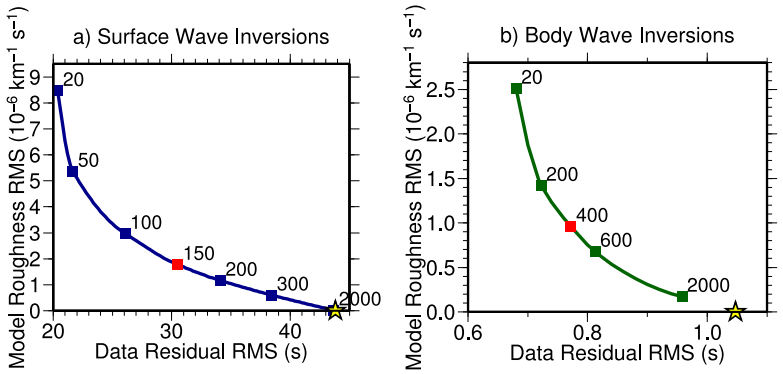

Figure 7. Trade-off curves between model roughness and rms residual for different damping parameters for (a) surface waves and (b) body waves. Roughness is calculated from the perturbations imposed on the model; hence the initial roughness (yellow star) is zero. Numbers indicate the damping parameters used. The optimum damper is 150 s^2 km^{-2} for the surface waves and 400 s^2 km^{-2} for the body waves (red squares). In this case the surface wave model is updated only above 100 km.

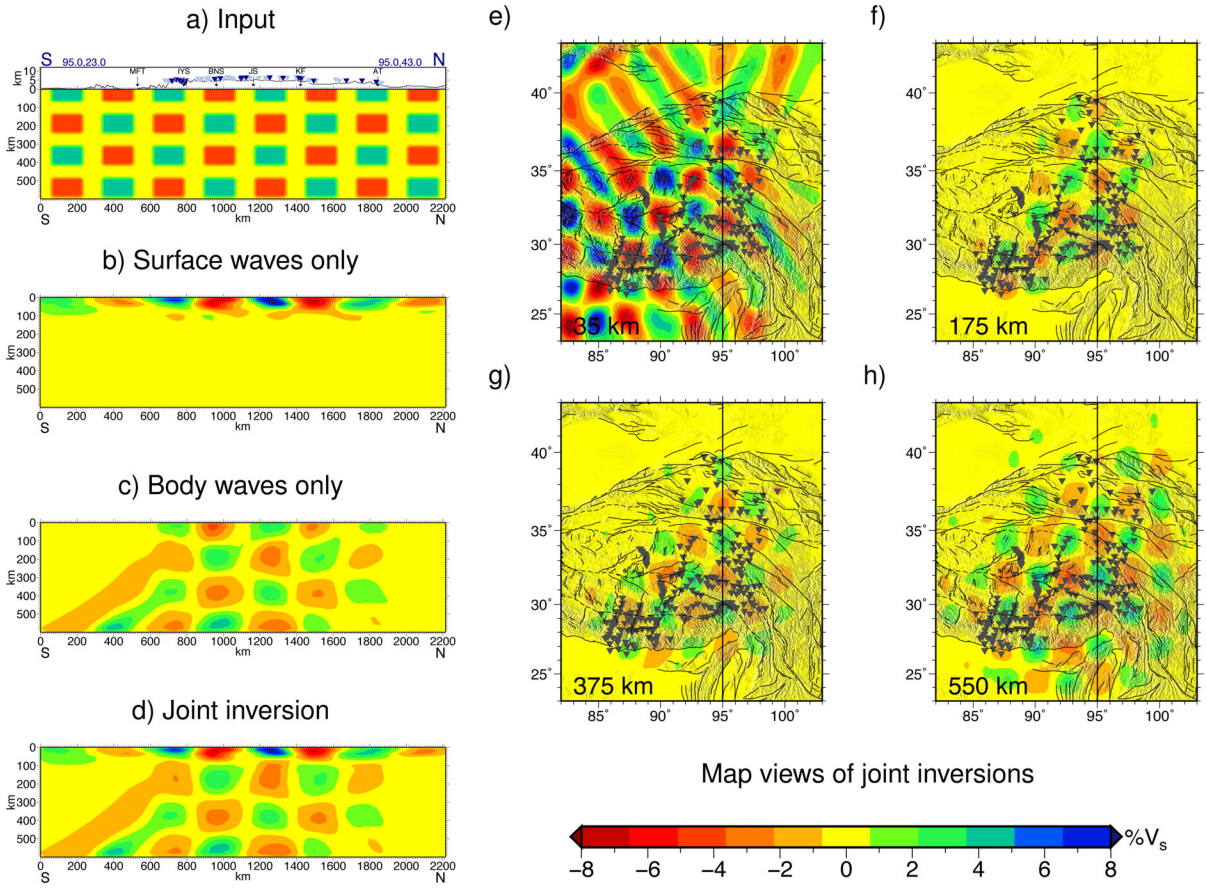

Figure 8. Checkerboard model with ±5 per cent anomalies used to tune the joint inversion. (a) Input model along 95°E. Model recovered using (b) only surface waves, (c) only body waves and (d) using both body waves and surface waves. Panels (e)–(h) are map views of the joint inversion at 35, 175, 375 and 550 km depth. Note that poor ray crossing coverage results in poor resolution in the north at shallow depths.

and so Barron & Priestley (2009) argue that the lower frequencies are blocked in the northern plateau due to a temperature inversion caused by heating the lower crust and upper mantle. Therefore, observations of S_n propagation agree well with our observation that the northern plateau is slower than the south at depths of 75 and 100 km (Figs 14a and b), with the slowest velocities seen in the north-central region. In a study of P_n velocities, Liang & Song (2006) show a generally similar pattern to our results at 75 km (Fig. 14a), with the northern plateau slower than the south. In addition, they see a belt of slow velocities reaching from the northern plateau to the Himalaya at ∼90°E, which may correspond to the slow velocities which we see along L2 at 75 km depth (Figs 13d and 14a). At the same time, this pattern is not observed in the study of S_n blockage of Barron & Priestley (2009).

4.2 Subducting 'wedge' in central Tibet

In contrast to the variations above 100 km (Figs 14a and b), velocities below 150 km are generally faster beneath the southern plateau

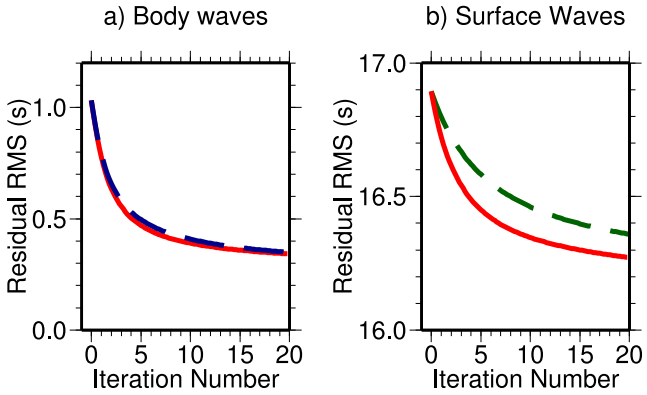

Figure 9. (a) Reduction in residuals for the checkerboards for (a) body wave data for the joint inversion (red line) and body wave only inversion (blue dashed line) and (b) surface wave data for the joint inversion (red line) and the surface wave only inversion (green dashed line).

than they are to the north (Fig. 14c). There is a relatively simple pattern in central Tibet, with a wedge of fast material extending from the Himalaya, where it dips at an angle shallower than ∼40°, to just north of the BNS (Figs 13a–c and Fig. 16: central profile). This feature is commonly interpreted as underthrusting Indian lithosphere (e.g. Kind *et al.* 2002; Li *et al.* 2008; Chen *et al.* 2010; Mechie & Kind 2013). Tilmann *et al.* (2003) observed steeply dipping fast velocities from 100 to 300 km depth in the northern Lhasa terrane in central Tibet (at ∼90°E). The fast velocities that we observe at this location are only below 300 km (Figs 13j–l and 14c and d).

The synthetic tests show that we should be able to recover a wedge of fast velocities at these depths reasonably well (Fig. 12a). Nevertheless, we explore five other scenarios that could potentially generate a similar image: (1) subduction of constant thickness lithosphere dipping at ∼25°(Fig. 12b), (2) flat underthrusting with a small lithospheric drip (Fig. 12c), (3) flat underthrusting reaching underneath the entire plateau (Fig. 12d), (4) vertical subduction (Fig. 12e) and (5) subduction in addition to a flat area underneath the central plateau (Fig. 12f). These results show that smearing can make it difficult to distinguish between a thickening wedge (Fig. 12a) and constant thickness subduction which is relatively shallow dipping (Fig. 12b). Similarly a wedge that was caused by flat underthrusting, followed by a subsequent lithospheric drip (Fig. 12c) would be indistinguishable from lithospheric thickening north of the collision zone. Very steep subduction would be likely to show up well (Fig. 12e), although smearing would be expected at the base. The synthetics also show that small gaps can occur in the retrieved structure, such as along profile L2 for some of the synthetic tests (Figs 12b, d and f: fourth column), despite good ray coverage along L2 (Fig. 3). A comparison between the results and synthetics (Figs 13b and 12) suggests that the Indian lithosphere underthrusts the plateau to approximately the BNS, and that there

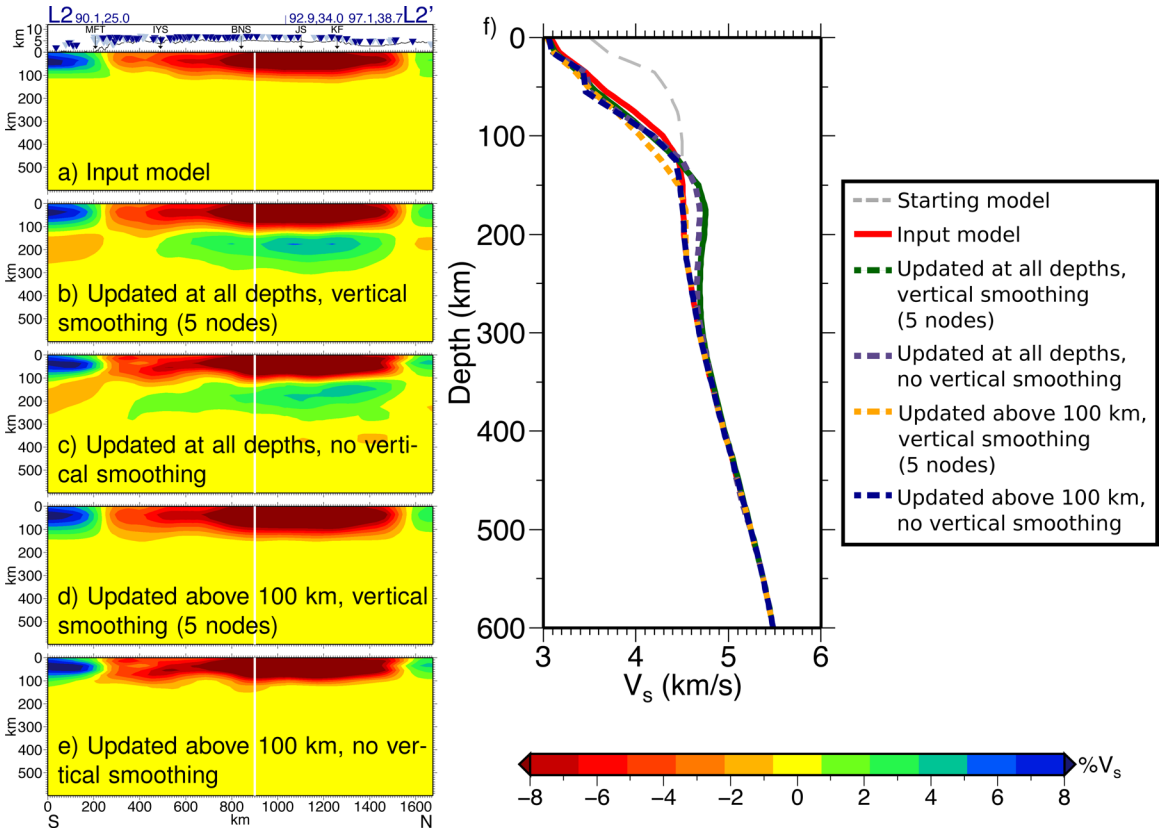

Figure 10. Initial tests showed that the surface wave analysis created artefacts in the 100–400 km depth range. The test shown here was devised to address this problem. The left column displays models along profile L2 (shown in Fig. 2), and the right panel (f) shows velocity–depth profiles of the same models (located 900 km along L2 and indicated by the white line). The input model mimics thickened crustal structure beneath the plateau, but with no laterally varying structure below 120 km (a and f: red line). The starting model for inversion is indicated by the dashed grey line in (f). Model recovered using smoothing across five nodes in each cardinal direction, and allowed to update at all depths (b and f: green line). Model recovered without vertical smoothing, and allowed to update at all depths (c and f: purple line). Model recovered with vertical smoothing across five nodes in each cardinal direction, but initially only allowed to update above 100 km (d and f: orange line). We find that we should invert without vertical smoothing and initially only update above 100 km before allowing updates to 150 km and then 200 km (e and f: blue line).

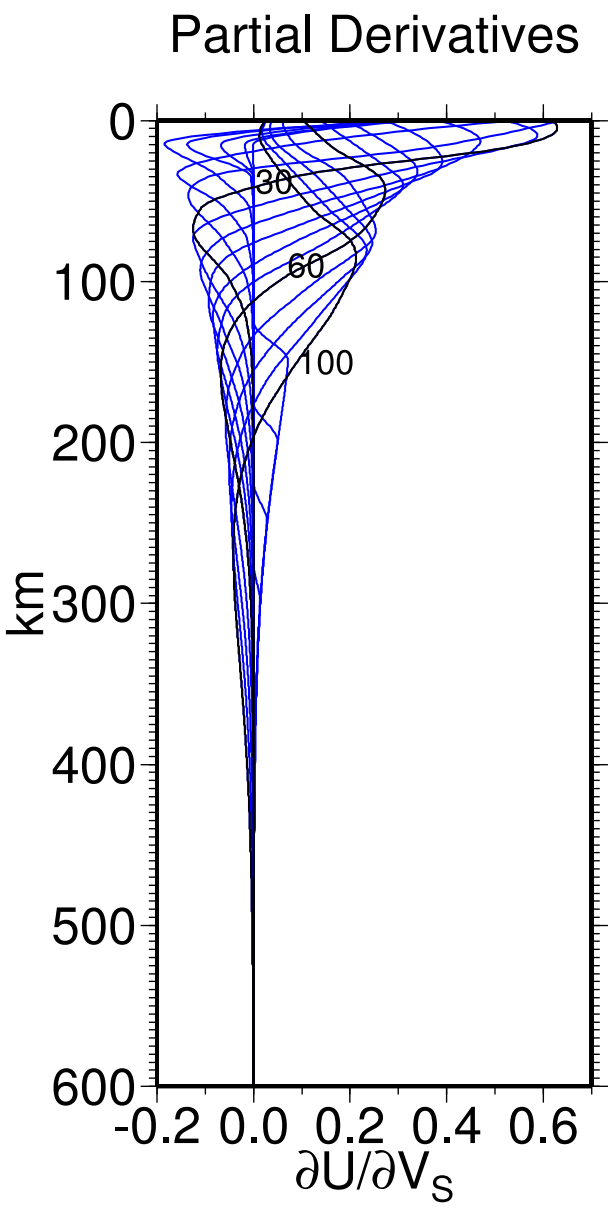

Figure 11. Partial derivatives of surface wave group velocity. A range of periods are shown from 4 to 100 s, with the 30, 60 and 100 s periods labelled.

may be some steeper subduction underneath this region, particularly at the northern edge (Fig. 16: central profile).

4.3 Complex structure in southeast Tibet

In map view, the faster velocities underneath the southern plateau appear broken by an area ∼300 km wide that stretches from the northern edge of central Tibet south-eastwards as far as the Himalaya (Fig. 14c, eastern profile and Fig. 16). Similarly, profile L2 (Figs 13d–f) shows fast velocities that reach as far as the XXF, but with a gap from 100 km to at least 150 km depth for ∼300 km beneath the IYS. This feature may extend to 300 km depth, although the percentage contrast is lower at these depths. We note that the percentage difference across the gap may not be well constrained, since the checkerboard tests indicate that it is possible to overestimate the relative amplitudes (Fig. 8 and Section 3.6). However, the absolute velocities from 100 to 150 km depth along L2 (Figs 13e and f) suggest that velocities within the gap are slow only in a relative sense. We find that the surface waves can help constrain the absolute average seismic velocities down to ∼150 km, with good constraints above 75 km (for further information see Fig. S2). The gap has been observed by previous investigators (Ren & Shen 2008; Liang *et al.* 2011, 2012; Zhang *et al.* 2012b).

A number of investigators have noted that many of the north–south rifts in southern Tibet (Fig. 1) occur above regions of slow velocities. The rifts are generally thought to be a consequence of the east–west extension of southern Tibet (e.g. Larson *et al.* 1999). It has been debated whether the rifts are restricted to the upper crust or involve the entire lithosphere (e.g. Masek *et al.* 1994; Yin 2000). Ren & Shen (2008) interpret the low-velocity gap as evidence of asthenospheric upwelling, which is then responsible for the surface rifting. There are a number of earthquakes which occur just above or below the Moho in southernmost Tibet, and also where the Moho dips beneath the Himalaya, the majority of these have a large strike-slip component (de la Torre *et al.* 2007). Liang *et al.* (2012) suggest that this makes it unlikely that the rifts have a particularly deep signature, and discuss a number of other possibilities, for example, that the low velocities are due to pre-existing compositional variation within the subducting Indian Plate. They prefer an explanation where low velocities are caused by upwelling mantle material which then fragments the subducting Indian Plate. As argued by Liang *et al.* (2012), the strength of the anomaly suggests a likely thermal origin. Of course, the thermal anomaly may follow pre-existing weaknesses. Alternatively, the gap could be due to the subducting plate breaking as a result of its dipping angle, which could allow asthenospheric material to upwell through the breaks.

One model for plateau uplift involves delamination or removal of the bottom part of the lithosphere due to Rayleigh-Taylor instabilities (e.g. Houseman *et al.* 1981; Molnar 1988). Delamination is inconsistent with our tomography further south, where we observe fast velocities in the uppermost mantle. However, such a process could potentially explain a narrow low-velocity gap as a small section that has dropped deeper into the mantle. Barron & Priestley (2009) argue that the lithospheric lid is present across the entire plateau, since low-frequency S_n waves propagate across it. Our tomographic model is consistent with either a narrow gap in the lithospheric lid or an intact lid which includes significantly faster regions associated with the subducting Indian Plate.

We suggest that the slow velocities occur because the angle of subduction steepens towards the eastern edge of the collision zone. This interpretation is consistent with a recent surface wave study of the upper 200 km beneath Tibet (Agius & Lebedev 2013), which finds that the Indian Plate subducts beneath eastern Tibet but underplates west-central Tibet and then subducts steeply. In our interpretation (Fig. 16), the gap in the fast velocities marks the northern edge of the Indian lithosphere (Figs 13d and 14c). Even so, there are a number of possible scenarios between which we cannot distinguish. For example, it could be possible that subduction has been occurring at a steeper angle in the northeast than in the west. Alternatively, the dip angle could have been relatively similar across the whole of Tibet, but the northeastern part of the lithosphere is presently rolling back. Although it is possible that there is a major north–south break in the subducting plate, neither of these scenarios require it.

4.4 The Qaidam Basin and eastern Tibet

Karplus *et al.* (2011) observe a Moho step ∼100 km north of the Kunlun Fault, where the crustal thickness is reduced from >70 km

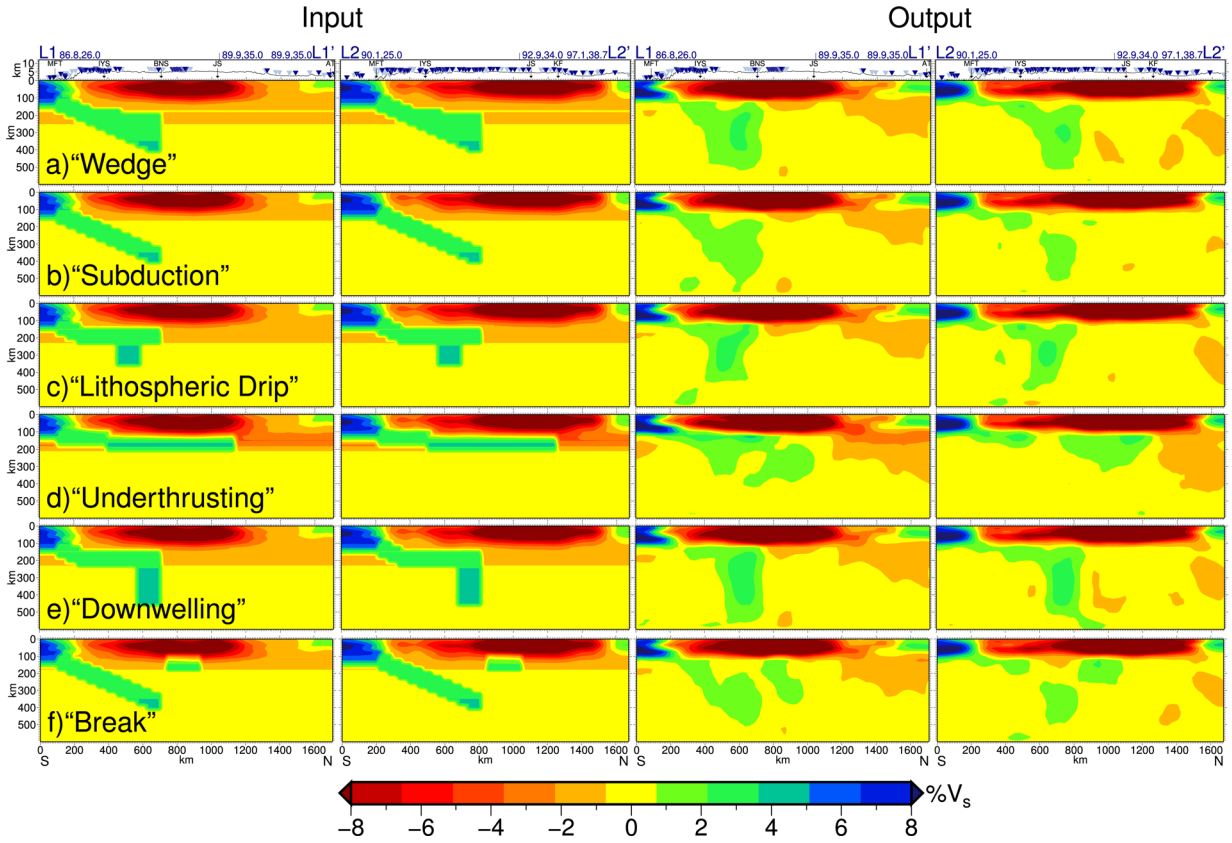

Figure 12. Six models designed as tests for the recovery of probable structures. The two columns on the left show the input models (along profile L1 and L2 and shown in Fig. 2) and the two columns on the right show the recovered models (also along L1 and L2), plotted as relative percentage anomalies. The top profiles show the topography and station distribution.

to ∼50 km within the basin. Other researchers (e.g. Yue *et al.* 2012) see a similar contrast. In our results, the 4.1 km s^{-1} contour is at ∼50 km below the basin, and >70 km across the rest of the plateau (Figs 13b, e and h). From ∼35 to 100 km depth below the Qaidam we see fast velocities relative to the rest of the plateau (Figs 13a, d and g). These are likely due to the shallower Moho as mantle material would be found at shallower depths. Karplus *et al.* (2011) suggest that crustal material may be injected underneath the southern edge of the Qaidam, as they observe crustal velocities below the Moho. We similarly see slow velocities dipping underneath the southern edge of the basin (Figs 13a,d and g).

The results show a wedge of fast velocities beneath southeastern Tibet along L3 (Fig. 13g). Unlike profile L2, these fast velocities appear to be continuous from mid-crustal depths underneath the Himalaya all the way to the XXF. The fast velocities reach further north here than in central Tibet, and the northern end of the wedge extends from ∼100 to 300 km depth. It is difficult to determine the root source of these northeastern fast velocities. On the one hand, they appear connected to the subducting Indian lithosphere underneath the Himalaya along profile L3. On the other, they are disconnected along profile L2. One possibility is that the northeastern fast velocities are thickened Asian lithosphere, which meets Indian lithosphere at some point along profile L3. Alternatively, all the fast velocities in the central part of profile L2 may represent underthrusting Indian lithosphere that has fragmented or broken off and dripped into the mantle.

Mechie & Kind (2013) note that, despite many differences in detail, most studies see fast upper-mantle velocities to about 100 km north of the BNS (e.g. Friederich 2003; Tilmann *et al.* 2003; Li *et al.* 2008; Feng *et al.* 2011; Liang *et al.* 2012), and that this is generally attributed to Indian lithospheric mantle underthrusting the plateau. A significant exception to this view is the surface wave model of Priestley *et al.* (2006), which images fast velocities underneath the entire plateau. The image shows fast velocities just to the north of the BNS along L1 in central Tibet (Fig. 13a). Along L2, we also see fast velocities underneath nearly the whole plateau (as far as the XXF), but with a narrow break (Fig. 13d). This break is likely to be too small for longer period surface wave studies, such as Priestley *et al.* (2006), to resolve, as their resolution limit is on the order 2°.

Tapponnier *et al.* (2001) proposed that there may be several parallel sets of southward-subducting Asian lithospheres beneath northern Tibet. The fast velocities that we see between the BNS and XXF along L2 and L3 suggest that this may be possible in northeast Tibet. However, as the synthetic tests suggest that vertical smearing over 150 km or more is possible in this region (Fig. 12), we are cautious about interpreting this feature as subduction. In any event, any subduction occurring here must be shallower than that observed for the Indian lithosphere in the south.

In common with a number of other researchers (e.g. Ceylan *et al.* 2012; Liang *et al.* 2012; Obrebski *et al.* 2012), we see slower velocities between the Qaidam and the rest of the plateau (Figs 13a, d and g). However, in our case, the slowest regions are confined to depths less than 100 km. By 150 km, the absolute velocities are not particularly slow (less than 2 per cent slower than *ak135*). The slower velocities argue against subduction of the Qaidam beneath the plateau.

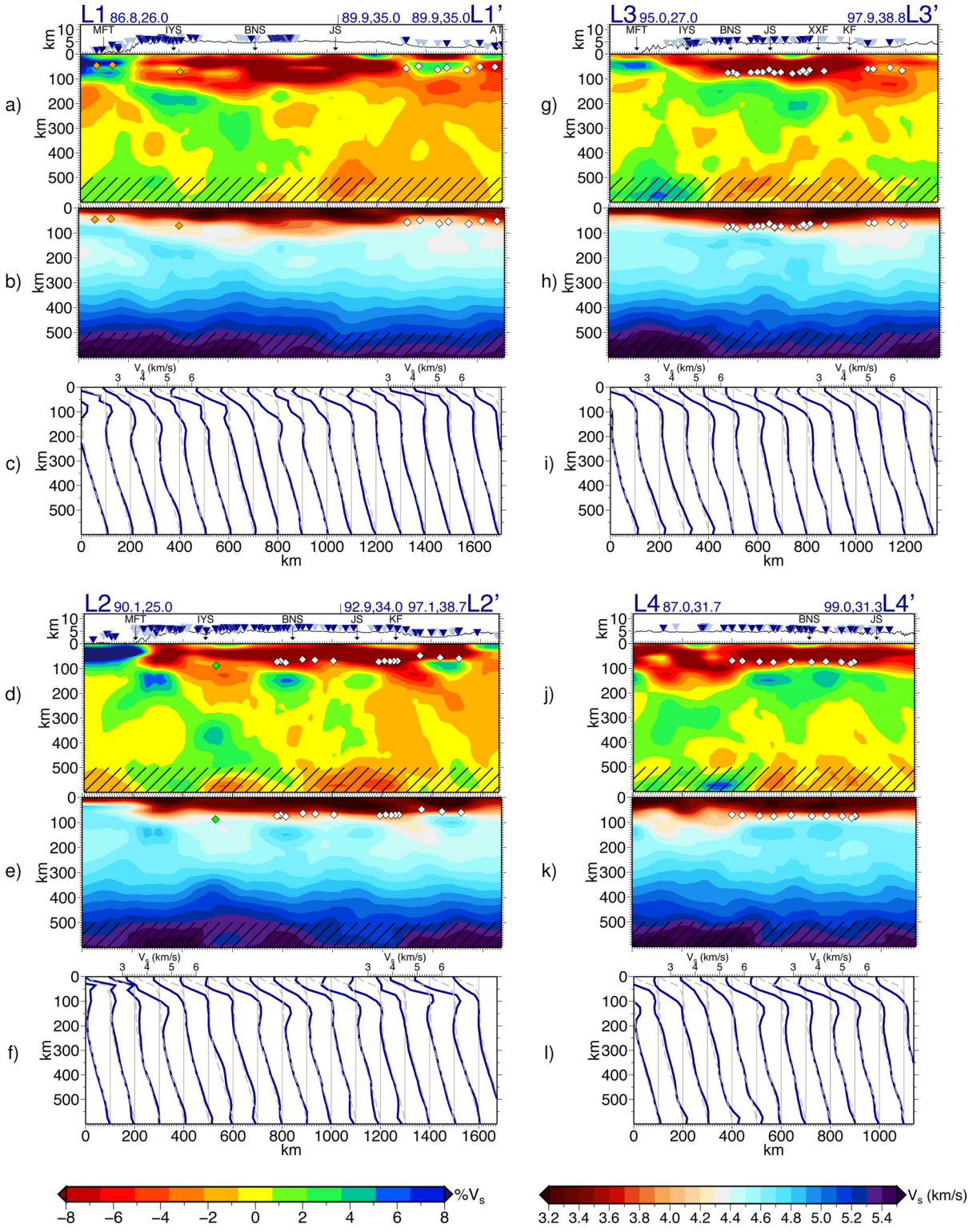

Figure 13. The results of the joint inversion along profiles L1 (a, b, c), L2 (d, e, f), L3 (g, h, i) and L4 (j, k, l). In each profile, the results are plotted as relative percentage anomalies (a, d, g, j), as absolute shear wave velocities (b, e, h, k) and as a velocity–depth profile every 100 km along the profile (c, f, i, l). For the velocity–depth profiles the blue lines show the results, and the dashed grey lines show the velocities of the starting model ('smoothed *ak135*'). The grid lines show the location of each profile (the grid line also corresponds to 4.5 km s^{-1}). Body wave stations, topography and larger faults and sutures are projected onto the profile (the same as in Fig. 3). Note that the body waves are not sensitive to absolute velocity, and therefore absolute velocities should be used as a guide only. Also note that the relative anomalies are relative only to the average velocity at that depth. Moho depths (within 100 km of the profile) are shown by diamonds: green diamonds are those estimated using receiver functions only (Mitra *et al.* 2005), white diamonds are estimated using the slant-stack method (Yue *et al.* 2012) and orange diamonds are estimated from a surface wave and receiver function joint inversion (Acton *et al.* 2011). The hashed area indicates a region where anomalies outside of the modelled region may be potentially mapped into the base of the model. Map views of the results and the location of the profiles are shown in Fig. 14.

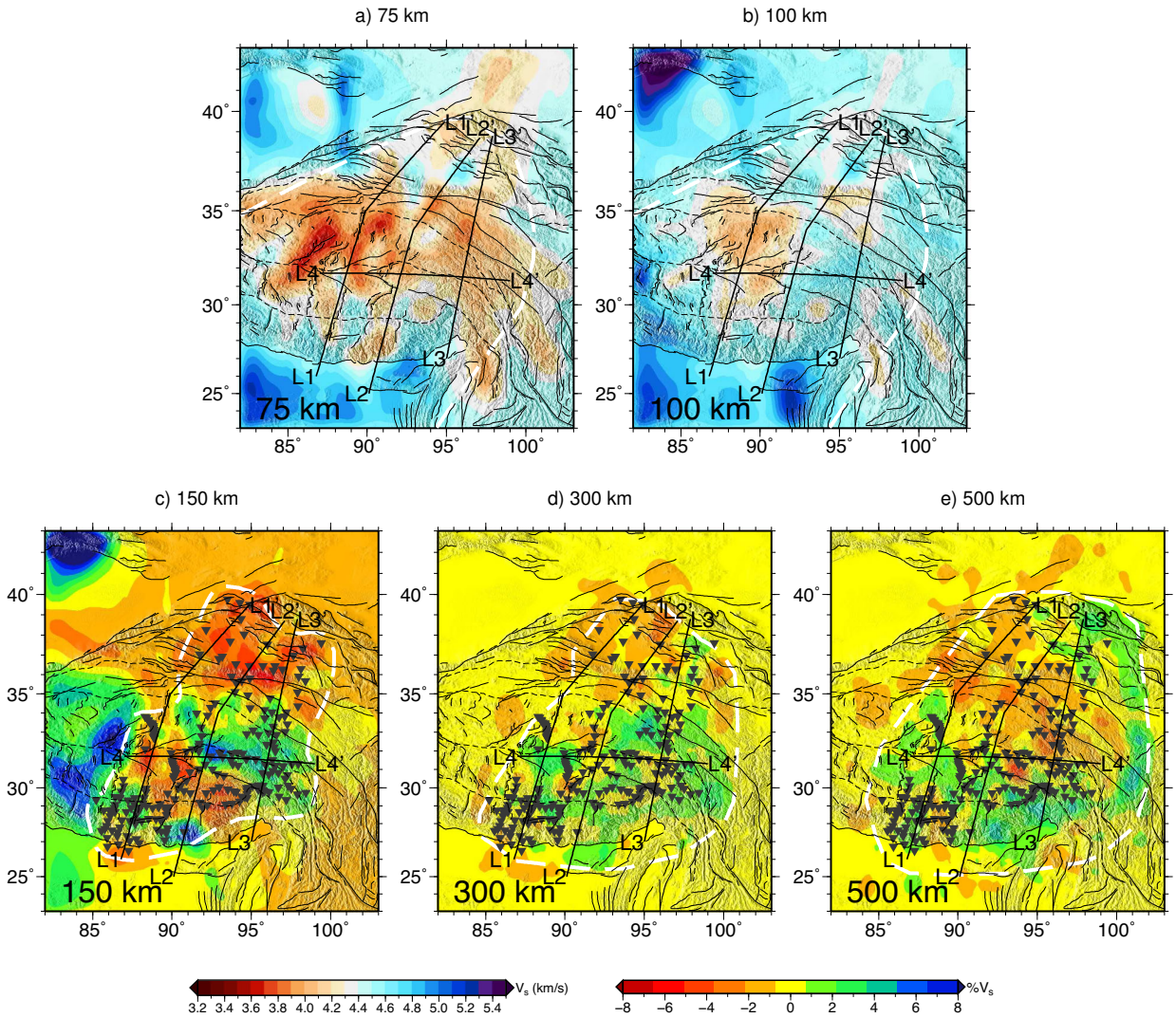

Figure 14. Map views of the joint inversion results at 75, 100, 150, 300 and 500 km depth. The 75 and 100 km plots show absolute shear wave anomalies while the 150, 300 and 500 km are relative percentage anomalies. The white dashed lines indicate the edge of well-resolved coverage. The body wave stations are shown as grey triangles in the deeper sections. The average velocities from shallowest to deepest sections are 4.39, 4.55, 4.56, 4.69, and 5.24 km s^{-1}. Additional depths are shown in Fig. S1.

4.5 Mantle structure below 400 km

The images reveal fast structures below 400 km across much of the south to as far north as the BNS along L1, and to the IYS along L2 and L3 (Figs 13a, d and g). Obrebski *et al.* (2012) also image a fast structure in the lower mantle at this location. Along L1 and L2, these fast structures may be connected to similar structures subducting beneath the Himalaya (Figs 13a and d), although along L3 they appear to be detached from the fast velocities above (Fig. 13g). We caution that these anomalies could be influenced by anomalies below the model region, and moreover, we would not expect excellent resolution at these depths. Nevertheless, these anomalies could be the result of an earlier stage of the collision that has been slowed down or stalled at the transition zone. van Hinsbergen *et al.* (2011) show a general north-eastwards motion of India over the past ∼50 Ma. Therefore, material accumulating above the transition zone could be left behind and now be observed southwards of any present subduction.

The model is not deep enough to determine whether or not a slab has penetrated through the transition zone. However, both the 410 and 660 mantle discontinuities have been imaged (Kind *et al.* 2002; Zhao *et al.* 2011) and are roughly parallel to each other beneath the whole of the plateau along the Lhasa to Golmud highway. Mechie & Kind (2013) suggest that this implies that there is no subducting slab penetrating into the mantle transition zone beneath the plateau, although this inference does not corroborate the tomography images of Li *et al.* (2008). Consistent with other studies, we see a south-to-north decrease in velocity: Mechie & Kind (2013) suggest that this is the cause of an apparent 20 km deepening of both the 410 and 660 km discontinuities in the northern part of the plateau.

4.6 Assessment of the joint inversion

The final models show a 65 per cent reduction in rms residual for the body waves and 87 per cent for the surface waves (Figs 18a and b) and improvements to the fit are seen for all periods (Fig. 18c). We find that the fit to both the surface wave and body wave observations is not degraded when we invert jointly. This suggests that by combining data sets we are reducing the model ambiguity in each of the individual data sets.

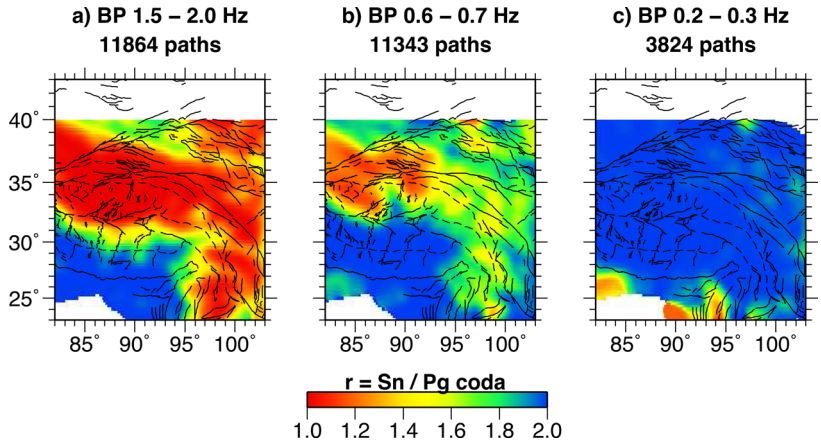

Figure 15. Maps of mean S_n propagation efficiency from Barron & Priestley (2009). The propagation efficiency is measured as the ratio r between the S_n phase and the Pg coda [$r = Sn$/(Pg coda)]. The data are displayed within various passbands, from higher to lower frequencies. The passbands and number of paths used to construct the maps are displayed above each map. Any paths with $r > 2$ or $r < 1$ were clipped to $r = 2$ and 1, respectively, when constructing the maps. The data are gridded in 0.25° cells, then a Gaussian filter with a radius of 150 km is applied. These maps corroborate the results of Figs 14(a) and (b) that indicate slow velocities in the uppermost mantle beneath the northern part of the plateau, with the slowest velocities in the north-central region.

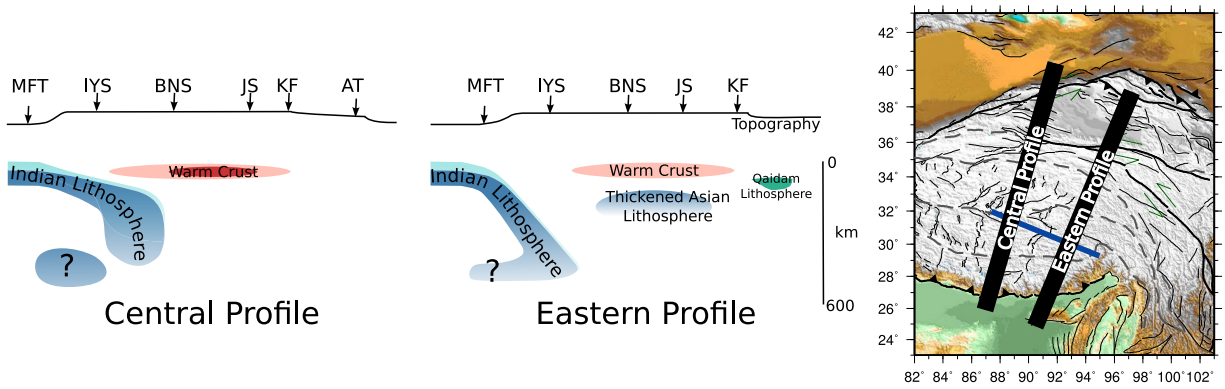

Figure 16. In the preferred interpretation of the joint inversion results, the Indian lithosphere underthrusts the plateau to approximately the BNS in central Tibet, and then subducts steeply (left-hand side). In eastern Tibet, the Indian lithosphere subducts at an angle of ∼45°. There are deep structures which may be related to an earlier phase of the collision. In eastern Tibet, there is thickened lithosphere which is likely to be Asian in origin. The warmest areas within the thickened Tibetan crust are in north-central Tibet. A fast region is seen below the Qaidam Moho (this is likely to be due to the shallower Moho beneath the basin). The location of the central and eastern profiles are shown on the elevation map of Tibet (right-hand side). The blue line indicates the inferred northern edge of Indian lithosphere at 150 km depth. Modified from Agius & Lebedev (2013).

Fig. 18(a) shows the body wave fit is close to the estimation of the measurement errors (Section 3.1). For the surface waves, the estimation of the measurement errors is based on the variation at each node with the initial 2-D inversion (Section 3.4). The surface wave fit drops very slightly below this estimation (Fig. 18b). We suggest that it is likely to be due to a small underestimation of the true errors (since the method of estimating errors includes some of the assumptions that we make, such as great circle path propagation). Additionally, we note that the initial stage (Section 3.4) will remove some of the true variation in group velocities, and this is likely to be why we can achieve such a good fit. The group velocities predicted by the final model from the joint inversion provide a generally good match to the output of the 2-D surface wave inversion (Fig. 5). The main features, such as the contrast between the Indian Shield, the plateau and the Tarim Basin are well reproduced. Some smearing occurs, particularly across the north and east. Many of the smaller features are also well reproduced: slow velocities in the Qaidam at 10 s (Fig. 5a); fast mountains in the Kunlun at 10 s (Fig. 5a); slow velocities in the north central plateau at 80 s (Fig. 5d).

In Fig. 17, we show models created with surface waves and body waves alone. The joint inversion (Fig. 13b) is very similar to the surface wave model at shallow depths (Fig 17a). Although the body wave inversion (Fig 17b) recovers the same features as the joint inversion (Fig. 13a) at depth, the amplitude is lower and much more noisy. Note that we make no crustal correction for the body wave inversion or the joint inversion. Within the joint inversion, we allow the surface waves to provide a crustal model for the body waves to pass through.

5 CONCLUSIONS

With this model, we fit two very different sets of observations. We find that the surface waves show the variation in the crust and uppermost mantle velocities. This provides a crustal correction for the body waves, at depths where they have poor resolution due to low crossing-ray coverage. Consequently, we are able to provide high-quality mantle images. In our preferred interpretation the Indian lithosphere underthrusts the plateau to approximately the BNS in central Tibet, and then subducts steeply. In eastern Tibet, the Indian lithosphere subducts at an angle of ∼45°. We explain the belt of slow velocities (which stretches from the northern edge of central

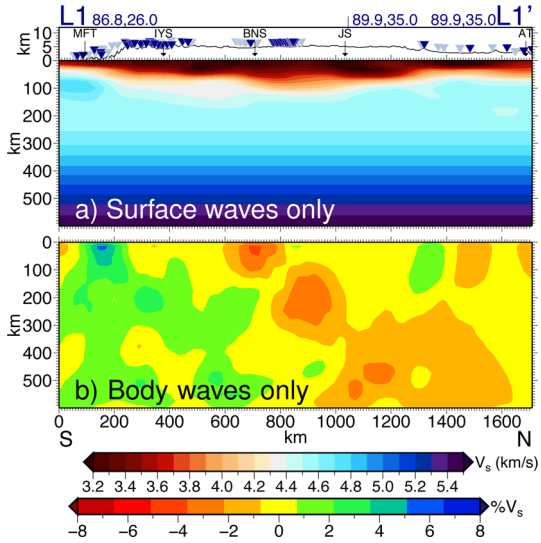

Figure 17. (a) Surface wave only inversion (plotted as absolute shear wave anomalies) and (b) body wave only inversion (plotted as relative percentage anomalies) along profile L1. All details are the same as in Fig. 13, which also shows the equivalent profile for the joint inversion.

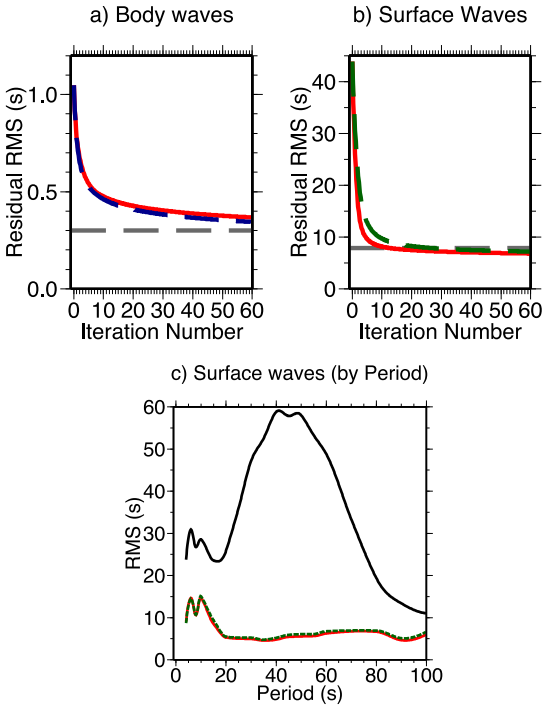

Figure 18. Reduction in the residuals for (a) the body wave data for the joint inversion (red line) and the body wave only inversion (blue dashed line) and (b) for the joint inversion (red line) and the surface wave only inversion (green dashed line). The dashed grey lines show the residual expected from the *a priori* estimation of the measurement errors; (c) rms residual for surface wave group traveltimes at each period. Initial residual (black), residual after inverting using surface waves only (green) and residual after the joint inversion (red).

Tibet south-eastwards as far as the Himalaya at 150 km depth) as marking the end of the Indian lithosphere at that depth. This is due to the steepening of the subduction zone. The fast velocities in the northeast are likely to be of a different origin, and probably represent thickened Asian lithosphere. Our results suggest that the process of accommodating the collision between India and Asia is more complex than might be expected from the uniformity of the plateau at the surface.

ACKNOWLEDGEMENTS

This study would not have been possible without permanent and temporary seismographs operated in Asia. Our study has included data from GSN (including IC, IU and II), China Digital Seismograph Network, GEOSCOPE, IRIS-IDA, Pacific-21, Kyrgyz Digital Network, Kyrgyz Seismic Telemetry Network and IRIS-USGS permanent seismic networks and the MANAS, Tien Shan Continental Dynamics, Tibetan Plateau Broadband Experiment, INDEPTH II, INDEPTH III, INDEPTH IV/ASCENT, HIMNT, Bhutan, Nanga Parbat Pakistan and GHENGIS PASSCAL temporary seismic deployments. We thank IIEES and LGIT for seismic data from Iran and also SEISUK for provision and assistance with instruments operated in northeast India. CN was supported by a Natural Environment Research Council studentship (grant NE/H52449X/1), with CASE funding from AWE Blacknest. We thank Nick Rawlinson and an anonymous reviewer for their constructive and helpful reviews. Figures were prepared with Generic Mapping Tools (GMT) software (Wessel & Smith 1998).

REFERENCES

Abers, G.A. & Roecker, S.W., 1991. Deep structure of an arc-continent collision: earthquake relocation and inversion for upper mantle *P* and *S* wave velocities beneath Papua New Guinea, *J. geophys. Res.,* **96**(B4), 6379–6401.

Acton, C.E., Priestley, K., Gaur, V.K. & Rai, S.S., 2010. Group velocity tomography of the Indo-Eurasian collision zone, *J. geophys. Res.,* **115**(B12), B12335, doi:10.1029/2009JB007021.

Acton, C.E., Priestley, K., Mitra, S. & Gaur, V.K., 2011. Crustal structure of the Darjeeling-Sikkim Himalaya and southern Tibet, *Geophys. J. Int.,* **184**(2), 829–852.

Agius, M.R. & Lebedev, S., 2013. Tibetan and Indian lithospheres in the upper mantle beneath Tibet: evidence from broadband surface-wave dispersion, *Geochem. Geophys. Geosyst.,* **14**(10), 4260–4281.

Aitchison, J.C., Ali, J.R. & Davis, A.M., 2007. When and where did India and Asia collide? *J. geophys. Res: Sol. Earth,* **112**(B5), 2156–2202.

Antolik, M., Gu, Y.J., Ekström, G. & Dziewonski, A.M., 2003. J362D28: a new joint model of compressional and shear velocity in the Earth's mantle, *Geophys. J. Int.,* **153**(2), 443–466.

Barron, J. & Priestley, K., 2009. Observations of frequency-dependent Sn propagation in Northern Tibet, *Geophys. J. Int.,* **179**(1), 475–488.

Ceylan, S., Ni, J., Chen, J.Y., Zhang, Q., Tilmann, F. & Sandvol, E., 2012. Fragmented Indian plate and vertically coherent deformation beneath eastern Tibet, *J. geophys. Res.,* **117**(B11), B11303, doi:10.1029/2012JB009210.

Chen, W.-P., Martin, M., Tseng, T.-L., Nowack, R.L., Hung, S.-H. & Huang, B.-S., 2010. Shear-wave birefringence and current configuration of converging lithosphere under Tibet, *Earth planet. Sci. Lett.,* **295**(1–2), 297–304.

Copley, A., Avouac, J.-P. & Royer, J.-Y., 2010. India-Asia collision and the Cenozoic slowdown of the Indian plate: implications for the forces driving plate motions, *J. geophys. Res.,* **115**(B3), doi:10.1029/2009JB006634.

Cotte, N., Pedersen, H., Campillo, M., Mars, J., Ni, J.F., Kind, R., Sandvol, E. & Zhao, W., 1999. Determination of the crustal structure in southern Tibet by dispersion and amplitude analysis of Rayleigh waves, *Geophys. J. Int.,* **138**(3), 809–819.

de la Torre, T.L., Monsalve, G., Sheehan, A.F., Sapkota, S. & Wu, F., 2007. Earthquake processes of the Himalayan collision zone in eastern Nepal and the southern Tibetan Plateau, *Geophys. J. Int.,* **171**(2), 718–738.

Feng, M., An, M., Zhao, W., Xue, G., Mechie, J. & Zhao, Y., 2011. Lithosphere structures of northeast Tibetan Plateau and their geodynamic implications, *J. Geodyn.,* **52**(5), 432–442.

Frederiksen, A., Bostock, M., VanDecar, J. & Cassidy, J., 1998. Seismic structure of the upper mantle beneath the northern Canadian Cordillera from teleseismic travel-time inversion, *Tectonophysics,* **294**(1–2), 43–55.

Friederich, W., 2003. The *S*-velocity structure of the East Asian mantle from inversion of shear and surface waveforms, *Geophys. J. Int.,* **153**(1), 88–102.

Gilligan, A., Roecker, S.W., Priestley, K.F. & Nunn, C. Shear velocity model for the Kyrgyz Tien Shan from joint inversion of receiver function and surface wave data, *Geophys. J. Int.,* in press.

Gomberg, J.S. & Masters, T.G., 1988. Waveform modelling using locked-mode synthetic and differential seismograms: application to determination of the structure of Mexico, *Geophys. J. Int.,* **94**(2), 193–218.

Graeber, F.M., Houseman, G.A. & Greenhalgh, S.A., 2002. Regional teleseismic tomography of the western Lachlan Orogen and the Newer Volcanic Province, southeast Australia, *Geophys. J. Int.,* **149**(2), 249–266.

He, R., Zhao, D., Gao, R. & Zheng, H., 2010. Tracing the Indian lithospheric mantle beneath central Tibetan Plateau using teleseismic tomography, *Tectonophysics,* **491**(1–4), 230–243.

Hermann, R.B. & Ammon, C.J., 2002. *Computer Programs in Seismology: Surface Waves, Receiver Functions and Crustal Structure,* Saint Louis Univ.

Hole, J.A. & Zelt, B.C., 1995. 3-D finite-difference reflection travel times, *Geophys. J. Int.,* **121**(2), 427–434.

Houseman, G.A., McKenzie, D.P. & Molnar, P., 1981. Convective instability of a thickened boundary layer and its relevance for the thermal evolution of continental convergent belts, *J. geophys. Res.,* **86**(B7), 6115–6132.

Hung, S.-H., Chen, W.-P., Chiao, L.-Y. & Tseng, T.-L., 2010. First multi-scale, finite-frequency tomography illuminates 3-D anatomy of the Tibetan Plateau, *Geophys. Res. Lett.,* **37**(6), L06304, doi:10.1029/2009GL041875.

Karplus, M.S., Zhao, W., Klemperer, S.L., Wu, Z., Mechie, J., Shi, D., Brown, L.D. & Chen, C., 2011. Injection of Tibetan crust beneath the south Qaidam Basin: evidence from INDEPTH IV wide-angle seismic data, *J. geophys. Res.,* **116**(B7), B07301, doi:10.1029/2010JB007911.

Kennett, B.L.N., Engdahl, E.R. & Buland, R., 1995. Constraints on seismic velocities in the Earth from traveltimes, *Geophys. J. Int.,* **122,** 108–124.

Kind, R. *et al.*, 2002. Seismic images of crust and upper mantle beneath Tibet: evidence for Eurasian plate subduction, *Science,* **298,** 1219–1221.

Larson, K.M., Bürgmann, R., Bilham, R. & Freymueller, J.T., 1999. Kinematics of the India-Eurasia collision zone from GPS measurements, *J. geophys. Res: Sol. Earth,* **104**(B1), 1077–1093.

Lebedev, S. & van der Hilst, R.D., 2008. Global upper-mantle tomography with the automated multimode inversion of surface and *S*-wave forms, *Geophys. J. Int.,* **173,** 1–14.

Lei, J. & Zhao, D., 2007. Teleseismic *P*-wave tomography and the upper mantle structure of the central Tien Shan orogenic belt, *Phys. Earth planet. Inter.,* **162**(3–4), 165–185.

Li, C., van der Hilst, R.D., Meltzer, A.S. & Engdahl, E.R., 2008. Subduction of the Indian lithosphere beneath the Tibetan Plateau and Burma, *Earth planet. Sci. Lett.,* **274**(1–2), 157–168.

Li, Z., Roecker, S., Wei, B., Wang, H., Schelochkov, G. & Bragin, V., 2009. Tomographic image of the crust and upper mantle beneath the western Tien Shan from the MANAS broadband deployment: possible evidence for lithospheric delamination, *Tectonophysics,* **477**(1–2), 49–57.

Liang, C. & Song, X., 2006. A low velocity belt beneath northern and eastern Tibetan Plateau from Pn tomography, *Geophys. Res. Lett.,* **33**(22), L22306, doi:10.1029/2006GL027926.

Liang, X., Shen, Y., Chen, Y.J. & Ren, Y., 2011. Crustal and mantle velocity models of southern Tibet from finite frequency tomography, *J. geophys. Res: Sol. Earth,* **116**(B2), B02408, doi:10.1029/2009JB007159.

Liang, X., Sandvol, E., Chen, Y.J., Hearn, T., Ni, J., Klemperer, S., Shen, Y. & Tilmann, F., 2012. A complex Tibetan upper mantle: a fragmented Indian slab and no south-verging subduction of Eurasian lithosphere, *Earth planet. Sci. Lett.,* **333–334,** 101–111.

Martin, M., Ritter, J.R.R. & the CALIXTO working group, 2005. High-resolution teleseismic body-wave tomography beneath SE Romania: I. Implications for three-dimensional versus one-dimensional crustal correction strategies with a new crustal velocity model, *Geophys. J. Int.,* **162**(2), 448–460.

Masek, J.G., Isacks, B.L., Fielding, E.J. & Browaeys, J., 1994. Rift flank uplift in Tibet: evidence for a viscous lower crust, *Tectonics,* **13**(3), 659–667.

McKenzie, D. & Priestley, K., 2008. The influence of lithospheric thickness variations on continental evolution, *Lithos,* **102,** 1–11.

McNamara, D.E., Owens, T.J. & Walter, W.R., 1995. Observations of regional phase propagation across the Tibetan Plateau, *J. geophys. Res.,* **100,** 22 215–22 230.

Mechie, J. & Kind, R., 2013. A model of the crust and mantle structure down to 700km depth beneath the Lhasa to Golmud transect across the Tibetan plateau as derived from seismological data, *Tectonophysics,* **606,** 187–197.

Mégnin, C. & Romanowicz, B., 2000. The three-dimensional shear velocity structure of the mantle from the inversion of body, surface and higher-mode waveforms, *Geophys. J. Int.,* **143**(3), 709–728.

Mitra, S., Priestley, K., Bhattacharyya, A.K. & Gaur, V.K., 2005. Crustal structure and earthquake focal depths beneath northeastern India and southern Tibet, *Geophys. J. Int.,* **160**(1), 227–248.

Mitra, S., Priestley, K., Gaur, V.K., Rai, S.S. & Haines, J., 2006. Variation of Rayleigh wave group velocity dispersion and seismic heterogeneity of the Indian crust and uppermost mantle, *Geophys. J. Int.,* **164,** 88–98.

Molnar, P., 1988. A Review of Geophysical Constraints on the Deep Structure of the Tibetan Plateau, the Himalaya and the Karakoram, and their Tectonic Implications, *Phil. Trans. R. Soc.: Math. Phys. Eng. Sci.,* **326**(1589), 33–88.

Molnar, P. & Tapponnier, P., 1975. Cenozoic tectonics of Asia: effects of a continental collision, *Science,* **189,** 419–426.

Montagner, J.-P., 1986. Regional three-dimensional structures using long-period surface waves, *Ann. Geophys.,* **4,** 283–291.

Ni, J. & Barazangi, M., 1983. High-frequency seismic wave propagation beneath the Indian Shield, Himalayan Arc, Tibetan Plateau and surrounding regions: high uppermost mantle velocities and efficient Sn propagation beneath Tibet, *Geophys. J. Int.,* **72**(3), 665–689.

Nolet, G., 1990. Partitioned waveform inversion and two-dimensional structure under the network of autonomously recording seismographs, *J. geophys. Res: Sol. Earth,* **95**(B6), 8499–8512.

Nunn, C. *et al.*, 2014. Imaging the lithosphere beneath NE Tibet: teleseismic P and S body wave tomography incorporating surface wave starting models, *Geophys. J. Int.,* **196**(3), 1724–1741.

Obrebski, M., Allen, R.M., Pollitz, F. & Hung, S.-H., 2011. Lithosphere-asthenosphere interaction beneath the western United States from the joint inversion of body-wave traveltimes and surface-wave phase velocities, *Geophys. J. Int.,* **185**(2), 1003–1021.

Obrebski, M., Allen, R.M., Zhang, F., Pan, J., Wu, Q. & Hung, S.-H., 2012. Shear wave tomography of China using joint inversion of body and surface wave constraints, *J. geophys. Res.,* **117**(B1), B01311, doi:10.1029/2011JB008349.

Paige, C.C. & Saunders, M.A., 1982. LSQR: an algorithm for sparse linear equations and sparse least squares, *ACM Trans. Math. Softw.,* **8**(1), 43–71.

Patriat, P. & Achache, J., 1984. India-Eurasia collision chronology has implications for crustal shortening and driving mechanism of plates, *Nature,* **311,** 615–621.

Priestley, K. & Tilmann, F.J., 2009. Relationship between the upper mantle high velocity seismic lid and the continental lithosphere, *Lithos,* **109,** 112–124.

Priestley, K., Debayle, E., McKenzie, D. & Pilidou, S., 2006. Upper mantle structure of eastern Asia from multimode surface waveform tomography, *J. geophys. Res.,* **111**(B10), B10304, doi:10.1029/2005JB004082.

Rapine, R., Tilmann, F., West, M., Ni, J. & Rodgers, A., 2003. Crustal structure of northern and southern Tibet from surface wave dispersion analysis, *J. geophys. Res.: Sol. Earth,* **108,** 2120, doi:10.1029/2001JB000445.

Rawlinson, N. & Fishwick, S., 2012. Seismic structure of the southeast Australian lithosphere from surface and body wave tomography, *Tectonophysics,* **572–573,** 111–122.
Rawlinson, N. & Kennett, B., 2008. Teleseismic tomography of the upper mantle beneath the southern Lachlan Orogen, Australia, *Phys. Earth planet. Inter.,* **167**(1–2), 84–97.
Rawlinson, N., Pozgay, S. & Fishwick, S., 2010a. Seismic tomography: a window into deep Earth, *Phys. Earth planet. Inter.,* **178**(3–4), 101–135.
Rawlinson, N., Tkalčić, H. & Reading, A.M., 2010b. Structure of the Tasmanian lithosphere from 3D seismic tomography, *Aust. J. Earth Sci.,* **57**(4), 381–394.
Ren, Y. & Shen, Y., 2008. Finite frequency tomography in southeastern Tibet: evidence for the causal relationship between mantle lithosphere delamination and the north–south trending rifts, *J. geophys. Res.: Sol. Earth,* **113,** B10316, doi:10.1029/2008JB005615.
Ritzwoller, M.H., Shapiro, N.M., Barmin, M.P. & Levshin, A.L., 2002. Global surface wave diffraction tomography, *J. geophys. Res.,* **107**(B12), doi:10.1029/2002JB001777.
Schmid, C., van der Lee, S., VanDecar, J.C., Engdahl, E.R. & Giardini, D., 2008. Three-dimensional S velocity of the mantle in the Africa-Eurasia plate boundary region from phase arrival times and regional waveforms, *J. geophys. Res.,* **113**(B3), B03306, doi:10.1029/2005JB004193.
Shapiro, N.M. & Ritzwoller, M.H., 2002. Monte-Carlo inversion for a global shear-velocity model of the crust and upper mantle, *Geophys. J. Int.,* **151,** 88–105.
Shedlock, K.M. & Roecker, S.W., 1987. Elastic wave velocity structure of the crust and upper mantle beneath the North China Basin, *J. geophys. Res: Sol. Earth,* **92**(B9), 9327–9350.
Stephens, C. & Isacks, B.L., 1977. Toward an understanding of Sn: normal modes of love waves in an oceanic structure, *Bull. seism. Soc. Am.,* **67**(1), 69–78.
Styron, R., Taylor, M. & Okoronkwo, K., 2010. Database of active structures from the Indo-Asian collision, *EOS, Trans. Am. geophys. Un.,* **91**(20), 181–182.
Tapponnier, P., Zhiqin, X., Roger, F., Meyer, B., Arnaud, N., Wittlinger, G. & Jingsui, Y., 2001. Oblique stepwise rise and growth of the Tibet plateau, *Science,* **294,** 1671–1677.
Taylor, M. & Yin, A., 2009. Active structures of the Himalayan-Tibetan orogen and their relationships to earthquake distribution, contemporary strain field, and Cenozoic volcanism, *Geosphere,* **5**(3), 199–214.
Tilmann, F. & Ni, J. the INDEPTH III Seismic Team, 2003. Seismic imaging of the downwelling Indian lithosphere beneath central Tibet, *Science,* **300,** 1424–1427.
VanDecar, J.C. & Crosson, R., 1990. Determination of teleseismic relative phase arrival times using multi-channel cross correlation and least squares, *Bull. seism. Soc. Am.,* **80,** 150–169.
van Hinsbergen, D.J.J., Steinberger, B., Doubrovine, P.V. & Gassmöller, R., 2011. Acceleration and deceleration of India-Asia convergence since the Cretaceous: roles of mantle plumes and continental collision, *J. geophys. Res.,* **116**(B6), B06101, doi:10.1029/2010JB008051.
Waldhauser, F., Lippitsch, R., Kissling, E. & Ansorge, J., 2002. High-resolution teleseismic tomography of upper-mantle structure using an a priori three-dimensional crustal model, *Geophys. J. Int.,* **150,** 403–414.
Wessel, P. & Smith, W.H.F., 1998. New, improved version of generic mapping tools released, *EOS, Trans. Am. geophys. Un.,* **79**(47), 579.
West, M., Gao, W. & Grand, S., 2004. A simple approach to the joint inversion of seismic body and surface waves applied to the southwest U.S., *Geophys. Res. Lett.,* **31**(15), L15615, doi:10.1029/2004GL020373.
Wittlinger, G. *et al.*, 1996. Seismic tomography of northern Tibet and Kunlun: evidence for crustal blocks and mantle velocity contrasts, *Earth planet. Sci. Lett.,* **139,** 263–279.
Yang, Y., Ritzwoller, M.H., Zheng, Y., Shen, W., Levshin, A.L. & Xie, Z., 2012. A synoptic view of the distribution and connectivity of the mid-crustal low velocity zone beneath Tibet, *J. geophys. Res.: Sol. Earth,* **117**(B4), B04303, doi:10.1029/2011JB008810.
Yin, A., 2000. Mode of Cenozoic east-west extension in Tibet suggesting a common origin of rifts in Asia during the Indo-Asian collision, *J. geophys. Res.,* **105**(B9), 21 745–21 759.
Yin, A. & Harrison, T.M., 2000. Geologic evolution of the Himalayan-Tibetan Orogen, *Ann. Rev. Earth planet. Sci.,* **28**(1), 211–280.
Yue, H. *et al.*, 2012. Lithospheric and upper mantle structure of the northeastern Tibetan Plateau, *J. geophys. Res.,* **117**(B5), B05307, doi:10.1029/2011JB008545.
Zhang, H., Zhao, D., Zhao, J. & Xu, Q., 2012a. Convergence of the Indian and Eurasian plates under eastern Tibet revealed by seismic tomography, *Geochem. Geophys. Geosyst.,* **13**, Q06W14, doi: 10.1029/2012GC004031.
Zhang, H., Zhao, J. & Xu, Q., 2012b. Crustal and upper mantle velocity structure beneath central Tibet by P-wave teleseismic tomography, *Geophys. J. Int.,* **190**(3), 1325–1334.
Zhao, W. *et al.*, 2011. Tibetan plate overriding the Asian plate in central and northern Tibet, *Nat. Geosci.,* **4**(12), 870–873.

SUPPORTING INFORMATION

Additional Supporting Information may be found in the online version of this article:

Figure S1. Results of the joint inversion. Sections below 125 km show relative percentage anomalies, while those above show absolute shear wave speeds. The white dashed lines indicate the edge of the well-resolved region. Body wave stations are indicated by grey triangles in the lower sections.
Figure S2. Velocity depth profiles through a checkerboard test. These profiles are located within the well-resolved area (i.e. within the white dashed lines on Fig. 14a) at (a) 90°E, 29°N and (b) 90°E, 32°N. The target model contains checkers of ±5 per cent perturbations (solid blue line) imposed on a background model (dashed blue line) that is 10 per cent slower than *ak135*. The starting model for the inversion is shown by the dashed grey line and corresponds to the 'smoothed *ak135*' model. The recovered model is indicated by the solid green line; the average of the recovered model is shown by the dashed green line.
(http://gji.oxfordjournals.org/lookup/suppl/doi:10.1093/gji/ggu193/-/DC1).

Please note: Oxford University Press is not responsible for the content or functionality of any supporting materials supplied by the authors. Any queries (other than missing material) should be directed to the corresponding author for the article.